Relationship between electrical conductivity anisotropy and fabric anisotropy in granular materials during drained triaxial compressive tests: a numerical approach

Qifei Niu, André Revil, Zhaofeng Li, Yu-Hsing Wang

Geophysical Journal International

Geophys. J. Int. (2017) **210,** 1–17
Advance Access publication 2017 April 6
GJI Rock and mineral physics, rheology

doi: 10.1093/gji/ggx140

Relationship between electrical conductivity anisotropy and fabric anisotropy in granular materials during drained triaxial compressive tests: a numerical approach

Qifei Niu,[1] André Revil,[2] Zhaofeng Li[3] and Yu-Hsing Wang[3]

[1] *Department of Petroleum Engineering, Colorado School of Mines, Golden, CO* 80401, *USA*
[2] *Université Savoie Mont-Blanc, ISTERRE CNRS, UMR CNRS* 5275, *F-*73376 *Le Bourget-du-Lac, France. E-mail: andre.revil@univ-smb.fr*
[3] *Department of Civil and Environmental Engineering, The Hong Kong University of Science and Technology, Clear Water Bay, Hong Kong, China*

Accepted 2017 April 5. Received 2017 April 3; in original form 2016 August 20

SUMMARY

The anisotropy of granular media and its evolution during shearing are important aspects required in developing physics-based constitutive models in Earth sciences. The development of relationships between geoelectrical properties and the deformation of porous media has applications to the monitoring of faulting and landslides. However, such relationships are still poorly understood. In this study, we first investigate the definition of the electrical conductivity anisotropy tensor of granular materials in presence of surface conductivity of the grains. Fabric anisotropy is related to the components of the fabric tensor. We define an electrical anisotropy factor based on the Archie's exponent second-order symmetric tensor **m** of granular materials. We use numerical simulations to confirm a relationship between the evolution of electrical and fabric anisotropy factors during shearing. To realize the simulations, we build a virtual laboratory in which we can easily perform synthetic experiments. We first simulate drained compressive triaxial tests of loose and dense granular materials (porosity 0.45 and 0.38, respectively) using the discrete element method. Then, the electrical conductivity tensor of a set of deformed synthetic samples is computed using the finite-difference method. The numerical results show that shear strains are responsible for a measurable anisotropy in the bulk conductivity of granular media. The observed electrical anisotropy response, during shearing, is distinct for dense and loose synthetic samples. Electrical and fabric anisotropy factors exhibit however a unique linear correlation, regardless of the shear strain and the initial state (porosity) of the synthetic samples. The practical implication of this finding confirms the usefulness of the electrical conductivity method in studying the fabric tensor of granular media. This result opens the door in using time-lapse electrical resistivity to study non-intrusively the evolution of anisotropy of soils and granular rocks during deformation, for instance during landslides, and to use the evolution of the conductivity tensor to monitor mechanical properties.

Key words: Electrical properties; Microstructure; Geomechanics; Electrical anisotropy.

1 INTRODUCTION

In the last three decades, electrical properties (electrical conductivity, streaming potential coupling coefficient and the material properties associated with induced polarization) have started to be used to monitor non-intrusively the evolution of mechanical properties of porous media (e.g. Arulanandan *et al*. 1981; Seladji *et al*. 2010; Revil *et al*. 2015). For instance, electrical conductivity and induced polarization can be used to monitor the compaction and shearing of granular porous materials including sands and shales (e.g. Hausenblas 1995; Abu-Hassanein *et al*. 1996; Rinaldi & Cuestas 2002; Koch *et al.* 2012). Self-potential can be used to monitor fracking operations and to determine the moment tensor of the seismic events (Mahardika *et al*. 2012; Haas *et al.* 2013). This has in turn applications to the monitoring of fracking, damage and healing, shearing and the compaction response of porous media with applications to the non-intrusive monitoring of slope stability, faults, volcanoes and landslides. Electrical resistivity exhibits much more sensitivity to anisotropy than other geophysical methods such as seismic (see discussion in Woodruff *et al*. 2015).

In this paper, we are interested in the evolution of anisotropy during shearing by simulating drained triaxial compression tests. Anisotropy is indeed a key characteristic of sheared granular materials. It reflects the evolution of the petrofabric of the porous material with time until a critical state is reached. The evolution of anisotropy is in turn closely related to the spatial arrangement of the grains,

pores and grain-to-grain contacts (contiguity). Anisotropy varies during deformation because volumetric and shear strains can induce changes in the microstructure of the materials (e.g. Cambou *et al.* 2004; Guo & Zhao 2013), especially in the discontinuities between the grains, which is described itself through a fabric tensor (Oda 1982). Fabric anisotropy (and its evolution during shearing) controls the directional nature of the shear strength, stress–strain behaviour and other geotechnical properties of granular soils (Rothenburg & Bathurst 1989; Collins & Muhunthan 2003) and can be understood by looking at the properties of the fabric tensor. Therefore, it is necessary to identify the role of fabric anisotropy in order to develop physics-based constitutive models in Earth sciences (Gao *et al.* 2010; Li & Dafalias 2012) and to apply geophysical methods to hydromechanical problems. The determination of granular media fabric tensor in the laboratory is usually based on the analysis of microstructural images of the porous materials, which can be obtained using advanced techniques such as neutron and X-ray microtomography (e.g. Viggiani *et al*. 2004; Andò *et al*. 2012; Kim *et al.* 2013) and scanning electron microscope images (e.g. Mirzababaei & Yasrobi 2007). However, these heavy techniques require sophisticated and costly equipments. This impedes their applications in most geotechnical laboratories and cannot be used up to now for soil samples undergoing deformation. They also cannot be used in field conditions. This is another motivation to use electrical methods in the laboratory or the field: these methods are easy to setup and very cheap. In addition, great progresses have been done in developing fully physics coupled inversion of electrical resistivity data (e.g. Jardani *et al*. 2013).

The electrical resistivity method has been extensively used to characterize soil and rock properties such as porosity, moisture content, hydraulic conductivity and Atterberg limits just to cite few examples (e.g. Abu-Hassanein *et al.* 1996; Rinaldi & Cuestas 2002; Bryson 2005). Some researchers have also explored the possibility of using directional conductivity measurements to study the inherent and induced anisotropy of soil and sedimentary rock fabrics (Arulanandan & Kutter 1978; Anandarajah *et al.* 1996; Kuganenthira *et al.* 1996; Friedman & Jones 2001; Wong 2003; Woodruff *et al.* 2015). The relationship between electrical and fabric anisotropies seems intuitive because the electrical conductivity of soils and granular media in general is strongly dependent on both the pore (grain) shapes and spatial arrangements (Mendelson & Cohen 1982; Friedman 2005). Both properties are known to control the fabric of granular porous media. Considering that the measurement of electrical conductivity of porous samples is relatively easy and low cost in both the laboratory and the field, we believe it could be a promising technique for the study of the fabric anisotropy in geotechnical engineering and geosciences.

Despite this potential, two issues need to be clarified if we want to apply the electrical conductivity method to monitor fabric anisotropy. The key questions we want to answer in this paper are the following:

(1) What is the most appropriate definition of an electrical anisotropy tensor that would be tied to a fabric anisotropy tensor? A suitable electrical anisotropy factor is not yet available, and in practice, people use empirically different parameters to calculate electrical anisotropy. For example, the ratio of the measured directional effective conductivity, A_σ, is used to quantify electrical anisotropy (e.g. Anandarajah *et al.* 1996). In addition, the literature is populated by works in which Archie's law is improperly used, neglecting the effect of surface conductivity in the conductivity equation. Actually, the measured effective conductivity is related to two different conduction mechanisms. The first corresponds to the pore water conductivity, which should be divided by the formation factor in saturated conditions. The second corresponds to the surface conductivity and corresponds to conduction in the electrical double layer coating the surface of the grains (e.g. Revil 2012, 2013a,b).

(2) How can we assess the relationship between the electrical anisotropy factor and the fabric anisotropy factor? Although the existence of such a relationship was proposed by Kuganenthira *et al.* (1996), solid evidences are still needed, especially for granular media with different initial states (dense or loose). The lack of experimental evidences is mainly because the current methods to determine the fabric of porous media in the laboratory are costly. For instance, to determine soil fabric evolution during shearing, the entire triaxial apparatus has to be installed in the X-ray scan, which requires significant modifications to both equipments. In contrast, it is relatively easy to calculate the fabric and its anisotropy of synthetic samples using discrete element method (DEM) simulations (e.g. Rothenburg & Bathurst 1989; Yimsiri & Soga 2010; Guo & Zhao 2013). In general, DEM simulation is relatively computationally intensive, which could restrict the number of particles used in calculations. However, it can provide detailed information on the motion of geomaterials at particle level and therefore, with the availability of low-cost, high-performance computer, DEM simulation is increasingly used in geomechanics to explore mechanical properties of granular media (Scholtès *et al*. 2009; Scholtès & Donzé 2012). If the directional electrical conductivity can also be calculated for synthetic samples in DEM simulations, the numerical method could be a powerful tool to study the relationship between electrical and fabric anisotropies, which in turn has applications for field studies. This calls for the development of a virtual computational rock physics laboratory as advocated for instance by Dvorkin *et al.* (2011) for seismic, mechanical and electrical properties and more recently by Torskaya *et al.* (2014) and Shabro *et al.* (2014).

The objective of this study is therefore twofold: (1) a clear definition of the electrical anisotropy factor should be developed and (2) a numerical method for the study of the fabric/electrical anisotropy relationship should be achieved. We first discuss electrical conduction mechanisms in porous media. Based on this model, we define an electrical anisotropy tensor from which we can compute an electrical anisotropy factor. This factor needs to be analogous to the fabric anisotropy factor determined from the fabric tensor (Oda 1982). Afterwards, we present a numerical method to calculate the directional conductivity of granular media.

2 ELECTRICAL CONDUCTIVITY OF GRANULAR POROUS MEDIA

The electrical conductivity of a saturated granular porous medium has two contributions: (1) the ionic conduction through the interconnected pore space and (2) the surface conduction occurring along the mineral–fluid interface (see Fig. 1, e.g. Van Olphen & Waxman 1958). In this section, we introduce the conduction mechanisms in isotropic and anisotropic porous media saturated with a pore water solution containing a dissociated salt such as NaCl.

2.1 Conductivity in absence of surface conductivity

We first consider the case of a saturated granular material without surface conduction (for instance at very high salinity for which

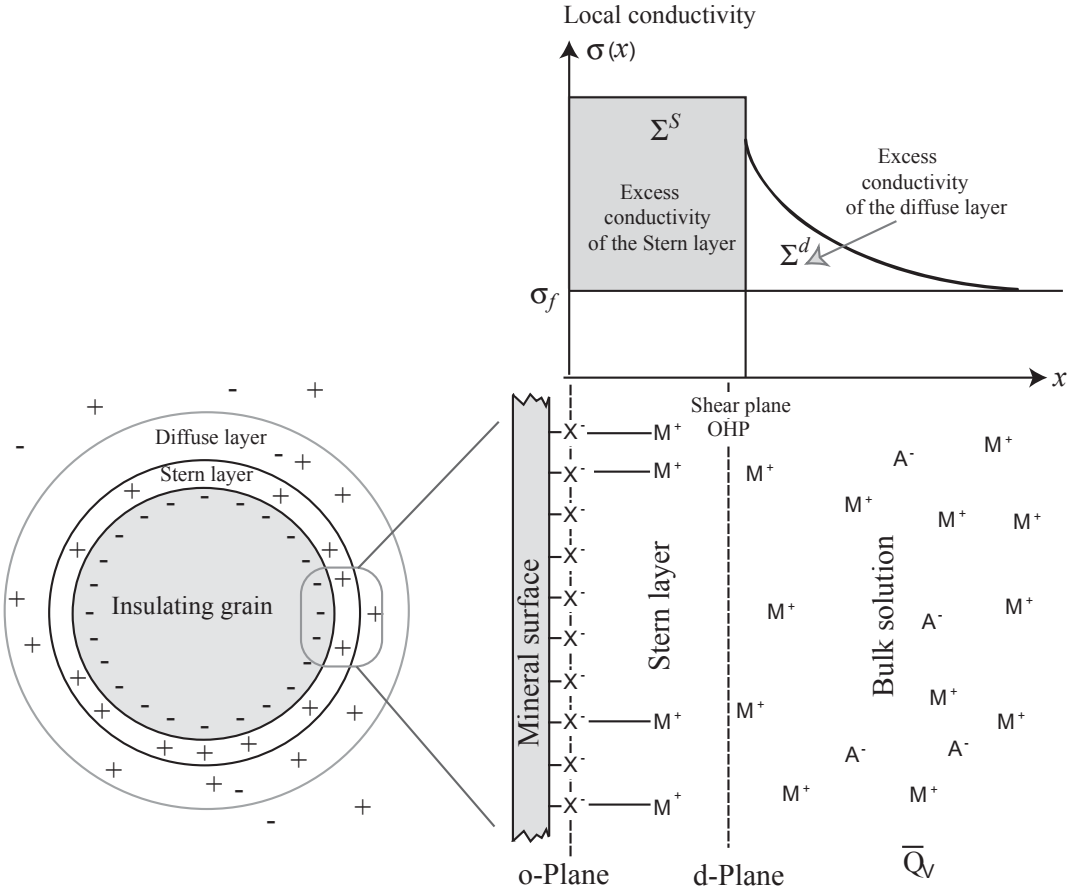

Figure 1. Sketch of the electrical double layer at the mineral–fluid interface coating a spherical grain of sand (modified from Revil & Florsch 2010). The mineral surface is usually charges due to protonation/deprotonation of the hydroxyl surface groups. The resulting fixed charge on the mineral surface (>*X*-sites) attracts the cations (counterions) and repels the anions (coions) in the vicinity of the mineral surface. The double layer comprises the Stern layer of sorbed counterions (forming inner or outer sphere complexes with the mineral surface) and a diffuse layer in which the concentrations of the counterions and coions obey Poisson–Botzmann distributions. The Stern and diffuse layers are characterized by anomalous conductivity with respect to the bulk pore water conductivity σ_w. These anomalous conductivities are characterized by the specific surface conductances Σ^{S} and Σ^{d} for the Stern and diffuse layers, respectively.

surface conductivity σ_{ss} may be negligible). In this case, the formation factor is defined by,

$$\lim_{\sigma_{\mathrm{ss}}=0} \sigma = \frac{1}{F}\sigma_w. \tag{1}$$

where σ and σ_w denote the electrical conductivity of the porous material and pore fluid, respectively, and F is called the (resistivity) formation factor. In the absence of surface conductivity, the conductivity problem is therefore defined by the following boundary-value problem involving the resolution of the Laplace equation for the electrical potential ψ defined through the pore space:

$$\nabla^2\psi = 0 \text{ in } V_p \tag{2}$$

$$\hat{\mathbf{n}} \cdot \nabla\psi = 0 \text{ on } S \tag{3}$$

$$\psi(z) = \begin{cases} \psi_1, \ z = 0 \\ \psi_1 + \Delta\psi, \ z = L \end{cases}, \tag{4}$$

where $\hat{\mathbf{n}}$ is the unit vector normal to the pore water/grain interface S, V_{p} denotes the interconnected pore volume and $\Delta\psi/L$ denotes a macroscopic electrical field applied for instance through cube of length L in the z-direction In absence of surface conductivity ($\sigma_{\mathrm{ss}} = 0$), the formation factor F is obtained by summing up the Joule dissipation of energy (e.g. Johnson & Sen 1988; Revil & Cathles 1999), that is,

$$\sigma\left(\frac{\Delta\Psi}{L}\right)^2 = \frac{1}{V}\int_{V_p} \sigma_w |\nabla\psi|^2 dV_p, \tag{5}$$

$$\sigma\left(\frac{\Delta\Psi}{L}\right)^2 = \frac{\sigma_w}{V}\int_{V_p} |\nabla\psi|^2 dV_p, \tag{6}$$

where the term dV_{p} denotes the integration is taken over the pore space. Therefore, the formation factor is given by Johnson & Sen (1988),

$$\frac{1}{F} = \frac{\sigma}{\sigma_w}, \tag{7}$$

$$\frac{1}{F} = \left(\frac{\Delta\Psi}{L}\right)^{-2}\frac{1}{V}\int_{V_p} |\nabla\psi|^2 dV_p. \tag{8}$$

It appears that $1/F$ is exactly an effective porosity in which more weight is given to the constrictions in which the local normalized electrical field $-\nabla\psi(\Delta\Psi/L)^{-1}$ is high (Revil & Cathles 1999). Note that F can be related to the connected porosity by Archie's law (Archie 1942),

$$F = \phi^{-m}, \tag{9}$$

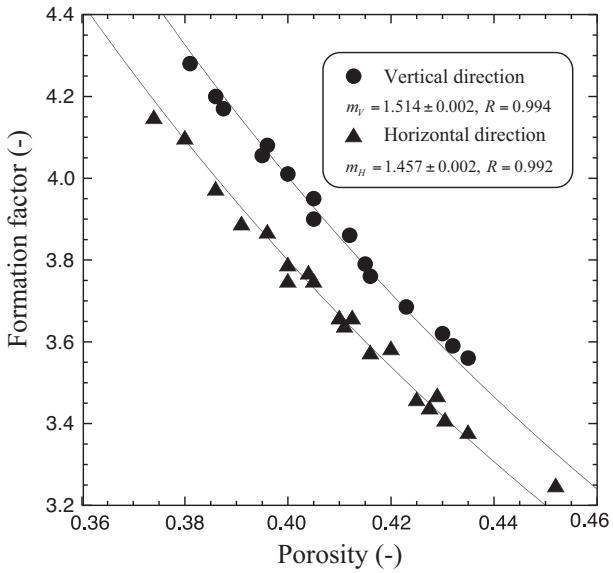

Figure 2. Formation factor porosity relationships for Monterey sand samples compacted with a variety of methods (pluviated, tapped and vibrated). The samples are transverse isotropic. Data from Arulanandan & Kutter (1978). The vertical and horizontal formations factors of the tensor **F** are fitted with Archie's law providing the values of the vertical and horizontal porosity exponents (m_V and m_H, respectively). The fits are materialized by the plain lines and the value of the correlation coefficients are provided.

where m is called the porosity exponent (also called cementation exponent in a number of publications). Sometimes, the data show the existence of a percolation threshold for granular media and Archie's law is replaced by $F = (\phi - \phi_p)^{-m}$ where ϕ_p denotes a percolation porosity (see, for instance Sen *et al*. 1981; Revil *et al*. 2014, for the Fontainebleau sandstone). For granular media, this exponent can be connected to the grain shape or grain shape distribution through the differential effective medium theory (Mendelson & Cohen 1982). For spherical grains in a random arrangement, the theory predicts that m is close to 1.5 in agreement with what is usually observed for granular media like well-rounded sands (Fig. 2).

2.2 Electrical double layer

Since the surface conductivity is often neglected in applied geophysics, it is worth recalling where this contribution comes from. The electrical double layer plays an important role for the contribution. As shown in Fig. 1, when a porous medium is immersed in an electrolyte, the mineral surface gets usually negatively charged at near-neutral pH values. The adjacent electrical double layer is formed of two layers namely the Stern and the diffuse layers. The Stern layer is located between the o-plane (mineral surface) and the d-plane (inner plane of the diffuse layer). The diffuse layer extends from the d-plane into the pore space. In Fig. 1, the element M^+ stands for cations (e.g. sodium Na^+), while A^- stands for anions (e.g. chloride Cl^-). For the counterions M^+ in the diffuse layer, their mobility is very close to the ions in the bulk water. In the Stern layer, the counterions are sorbed on the surface of aluminosilicates and silicates (van Olphen & Waxman 1958; Carroll *et al.* 2002). The local conductivity $\sigma(x)$ (in $S{\cdot}m^{-1}$) in the Electrical Double Layer depends on the local distance x from the mineral surface. The Stern layer contributes to the excess surface conductivity $\Sigma_s{}^{\mathrm{s}}$ (in Siemens, S) while the diffuse layer contributes to the excess surface conductivity $\Sigma_s{}^{\mathrm{d}}$ (in S, Revil & Florsch 2010, and Fig. 1). Because both

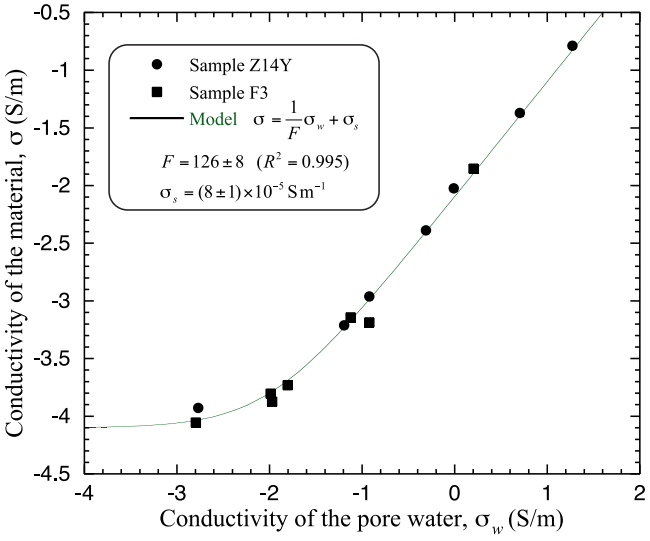

Figure 3. Conductivity versus pore water conductivity for the Fontainebleau sandstone (99.8 per cent pure silica). We use samples F3 (porosity 0.068, data from Börner 1992) and sample Z14Y (porosity 0.070, data from Revil *et al*. 2014). The electrical conductivity data for these two samples characterized by the same porosity and formation factor are consistent. The estimated surface conductivity and formation factor are 126 ± 8 and $(8 \pm 1) \times 10^{-5}$ S m^{-1}, respectively.

these terms have units of conductance, in this study we will term them specific surface conductances. Note also that while surface conductivity is very important in the presence of clay minerals, it is not negligible in clean sands and sandstones either as discussed recently by Revil *et al*. (2014). For instance, if the surface conduction cannot be neglected, the formation factor of Fontainebleau sandstones can be significantly smaller than their intrinsic formation factor (see their fig. 21).

2.3 Surface conductivity

We now consider the case when surface conduction exists. An example of surface conduction in a clay-free granular porous material (the Fontainebleau sandstone) is shown in Fig. 3. If conduction in the bulk pore space dominates, the surface conduction can be treated as a weak perturbation to the conduction in the bulk pore space (Johnson & Sen 1988) letting the electrical field distribution nearly unchanged. In this case, the effective conductivity of the porous medium σ is given by (see, for instance Bernabé & Revil 1995)

$$\sigma = \frac{1}{F}\sigma_w + \sigma_S, \tag{10}$$

where σ_s is the surface conductivity. An experimental data set such as shown in Fig. 3 is usually used to determine the formation factor and the surface conductivity. Two things need to be appreciated: (1) eq. (10) describes a high salinity asymptotic behaviour and for very low salinity, it is better to use a differential effective medium theory to capture the non-linearity between σ and σ_w (see discussions in Bernabé & Revil 1995; Niu *et al*. 2016 and references therein). (2) In this high salinity asymptotic behaviour, the formation factor F is not defined anymore as the ratio between the pore water conductivity and the rock sample conductivity (this ratio can be defined eventually as an apparent formation factor, but its usefulness is questionable since it depends on salinity, e.g. Revil *et al*. 2014).

The surface conductivity σ_s (at the macroscopic scale) should not be confused with the specific surface conductivity σ_{ss} (at the grain

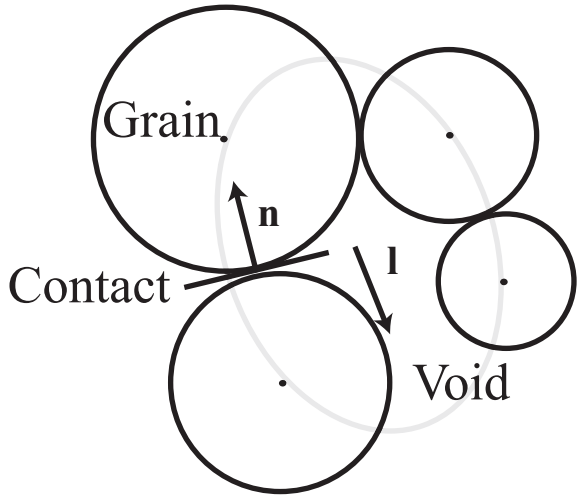

Figure 4. Sketch of the unit vectors defined for the grain-to-grain contacts and voids. The ellipse is the void cell ellipse connecting the centres of the grains. The unit vectors **n** and **l** are defined at the grain-to-grain contact and along the void ellipse, respectively.

scale), which is the equivalent electrical conductivity of the solid phase associated with the specific surface conductance Σ_s (Fig. 1). Revil & Glover (1997) extended the use of the Joule dissipation theorem to the case of bulk and surface conduction. The macroscopic Joule dissipation of energy is the sum of all the Joule dissipation contributions occurring at the microscopic scale in both the bulk pore water and in the electrical double layer. This yields,

$$\sigma\left(\frac{\Delta\Psi}{L}\right)^2 = \frac{1}{V}\int_{V_p}\sigma_w|\nabla\psi|^2dV_p + \frac{1}{V}\int_S \Sigma_S|\nabla\psi|^2dS, \tag{11}$$

$$\sigma\left(\frac{\Delta\Psi}{L}\right)^2 = \frac{\sigma_w}{V}\int_{V_p}|\nabla\psi|^2dV_p + \frac{\Sigma_S}{V}\int_S|\nabla\psi|^2dS, \tag{12}$$

where Σ_S describes the specific surface conductivity of the electrical diffuse layer (in S; see Fig. 4). At high salinity (the Dukhin number defined by $\mathrm{Du} = F\sigma_s/\sigma_w \ll 1$, Shilov *et al.* 2001), the distribution of the electrical field is nearly the same as in absence of surface conductivity and we can write,

$$\sigma = \frac{\sigma_w}{F} + \left(\frac{\Delta\Psi}{L}\right)^{-2}\frac{\Sigma_S}{V}\int_S|\nabla\psi|^2dS, \tag{13}$$

which is similar to eq. (10). This provides an expression for the surface conductivity,

$$\sigma_S = \frac{2}{\Lambda F}\Sigma_S, \tag{14}$$

where

$$\frac{2}{\Lambda} = \frac{\int_S|\nabla\psi|^2dS}{\int_{V_p}|\nabla\psi|^2dV_p}, \tag{15}$$

denotes the characteristic pore size introduced by Johnson & Sen (1988). We can also write the total energy that is dissipated as,

$$\sigma\left(\frac{\Delta\Psi}{L}\right)^2 = \frac{1}{V}\int_{V_p}\sigma_w|\nabla\psi|^2dV_p + \frac{1}{V}\int_{V_p}\sigma_{\mathrm{ss}}|\nabla\psi|^2dV_s, \tag{16}$$

$$\sigma\left(\frac{\Delta\Psi}{L}\right)^2 \approx \frac{\sigma_w}{V}\int_{V_p}|\nabla\psi|^2dV_p + \frac{\sigma_{\mathrm{ss}}}{V}\int_{V_p}|\nabla\psi|^2dV_s, \tag{17}$$

and therefore the surface conductivity can also be written as,

$$\sigma_S \approx \frac{\sigma_{\mathrm{ss}}}{G}. \tag{18}$$

In the terminology used by Niu *et al.* (2016), this reciprocal formation factor G is defined by

$$\frac{1}{G} = \frac{1}{V}\left(\frac{\Delta\Psi}{L}\right)^{-2}\int_{V_s}|\nabla\psi|^2dV_s. \tag{19}$$

The parameter G is the formation factor of the porous medium if the associated solid and liquid phases are interchanged, and it can be defined in the way similar to the definition of F. In Revil & Cathles (1999), it is approximately given by $(1-1/F)\approx 1$. Taking now the two expressions of the surface conductivity, we have,

$$\sigma_{\mathrm{ss}}\int_{V_s}|\nabla\psi|^2dV_s \approx \Sigma_S\int_S|\nabla\psi|^2dS, \tag{20}$$

$$\sigma_{\mathrm{ss}} \approx \Sigma_S\frac{\int_S|\nabla\psi|^2dS}{\int_{V_s}|\nabla\psi|^2dV_s}. \tag{21}$$

It follows that the conductivity of the grains can be written as

$$\sigma_{\mathrm{ss}} \approx \Sigma_S\frac{2}{\Pi}, \tag{22}$$

where the quantity Π is defined by

$$\frac{2}{\Pi} \approx \frac{\int_S|\nabla\psi|^2dS}{\int_{V_s}|\nabla\psi|^2dV_s}, \tag{23}$$

and denotes a characteristic grain size. For spherical grains, the characteristic grain size Π is equal to the radius of the sphere (Niu *et al.* 2016).

The specific surface conductance is contributed by the electrical double layer. At the high-frequency limit, both the Stern and the diffuse layers contribute, that is, $\Sigma_s = \Sigma^{\mathrm{s}} + \Sigma^{\mathrm{d}}$. At the low-frequency limit, the conduction is only from the diffuse layer, that is, $\Sigma_s = \Sigma^{\mathrm{d}}$ (e.g. see Leroy *et al.* 2008). In this study, we consider the direct current (DC) electrical conductivity of granular materials, that is, at the low-frequency limit, and therefore the specific surface conductance is solely from the diffuse layer. Thus, the specific surface conductivity is given by $\sigma_{\mathrm{ss}} = (2/\Pi)\Sigma^d$. The specific surface conductance presents the influence of the interfacial electrochemistry of the electrical diffuse layer (O'Konski 1960; Revil & Florsch 2010). It is related to the pore fluid chemistry (such as ion mobility, ionic strength, pH and pore fluid composition) and the surface mineralogy, for example, by the Stern layer polarization model (Leroy & Revil 2009; Revil 2012, 2013b),

$$\Sigma^d = Q_s\cdot\beta_{(+)}\cdot(1-f), \tag{24}$$

where Q_s (C m^{-2}) is the charge density on the mineral surface, $\beta_{(+)}$ (m^{2}s^{-1}V^{-1}) is the counterions mobility in the diffuse layer and the partition coefficient f (dimensionless) defines the relative fraction of ions in the Stern layer. Note that f is controlled by the fluid chemistry and the mineralogy of the porous medium (Leroy & Revil 2009; Revil 2012). Combining eqs (14), (18) and (22) yields the following expression for the surface conductivity,

$$\sigma_s = \frac{1}{H}\Sigma^d \tag{25}$$

where H is a textural quantity that averages the specific surface conductance over the synthetic sample scale. The following relationship

follows $1/H = 2/(G\Pi) = 2/(\Lambda F)$. In the case of G is close to 1, we have $\Pi \approx \Lambda F$, which is equivalent to eq. (11) in Revil & Cathles (1999).

2.4 Extension to anisotropic conditions

The previous model can be extended to anisotropic (transversely isotropic) conditions (e.g. Arulanandan & Kutter 1978; Revil *et al.* 2013). The bulk conductivity tensor associated with contribution from the pore water conductivity is

$$\sigma = [F_{ij}\,\sigma_w + H_{ij}\,\Sigma^d]\mathbf{x}_i \otimes \mathbf{x}_j, \tag{26}$$

$$\mathbf{F} = F_{ij}\,\mathbf{x}_i \otimes \mathbf{x}_j, \tag{27}$$

$$\mathbf{H} = H_{ij}\,\mathbf{x}_i \otimes \mathbf{x}_j, \tag{28}$$

where $\mathbf{x}_i$ (i = 1, 2, 3) denotes the basis vector of the Cartesian frame of reference, $\otimes$ represents the tensorial or dyadic product of two vectors and F_{ij} denotes the components of the (symmetric second-rank) formation factor tensor $\mathbf{F}$ for the bulk conductivity. The components of this tensor have the following form,

$$F_{ij} = \frac{\int |\nabla\psi_i|^2 dV_p}{\left(\Delta\Psi_j/L\right)^2 V} \tag{29}$$

where $\Delta\Psi_j$ is the applied (macroscopic) potential difference in the j-direction and$-\nabla\psi_i$ is the local electric field in the i-direction (in absence of surface conduction). Similarly, H_{ij} denotes the components of the (symmetric second-rank) geometrical factor tensor which upscales the specific surface conduction to the sample scale, and has the following form,

$$H_{ij} = \frac{\int |\nabla\psi_i|^2 dS}{\left(\Delta\Psi_j/L\right)^2 V}, \tag{30}$$

where $\nabla\psi_i$ denotes the i component of the vector $\nabla\psi$ with respect to the Cartesian coordinate x_i. Note that adding the surface and bulk pore water conductivities (e.g. eq. 26) is only a high salinity approximation as discussed for instance in Bernabé & Revil (1995). At low salinities, the relationship between the conductivity of the material and the conductivity of the pore water becomes non-linear (see for instance for soils Shainberg *et al.* 1980).

3 ANISOTROPY TENSORS

In this section, we first briefly introduce the definition of the fabric anisotropy. Then, we define the electrical anisotropy tensor based on the same criteria used for the definition of the fabric anisotropy. We also analyse, based on their definitions, the possible relation between fabric and electrical anisotropy tensors.

3.1 Fabric tensor

Different forms of fabric tensors have been developed to quantify the fabric of granular materials, and most of them are defined based on the intergrain contact normal directions (Oda 1982), grain orientations (Oda 1972; Anandarajah *et al.*1996; Fu & Dafalias 2015) or void (pore) orientations (Li & Li 2009; Ghedia & O'Sullivan 2012). Among these fabric tensors, the contact normal-based definition is usually used in geomechanics of granular media. Indeed, a contact force having a direction deviating from the grain-to-grain contact normal direction is more likely to cause intergrain sliding or rolling (Fu & Dafalias 2015), and thus lead to a strain change in the core sample. The void-based definition of the fabric tensor is used usually to characterize transport properties in the pore network such as the anisotropic permeability (Berkowitz & Ewing 1998). Finally, the grain orientation-based definition of the fabric tensor is more useful for soil deformation with elongated grains (Anandarajah 1994). These three definitions are strongly interrelated and numerical studies have confirmed a definite and linear correlation among them in granular materials with different densities and intergrain friction (Theocharis *et al.* 2014; Fu & Dafalias 2015). Such a correlation is also intuitive since the evolution of void spaces in granular materials results from the evolution of the solid phase and the evolution of the geometry of the grain-to-grain contacts.

The fabric tensor is based on the normal to fabric anisotropy tensor the contacts points or surfaces between the grains of the medium. As a frequently-used tensor to quantify the fabric of granular media, this second-order contact fabric tensor $\mathbf{T}^c$ (Oda 1976) is written as,

$$\mathbf{T}^c = \int_\Omega E(\mathbf{n})\,\mathbf{n} \otimes \mathbf{n} d\Omega. \tag{31}$$

where $\mathbf{n}$ is the unit vector representing the direction normal to the grain-to-grain contacts (Fig. 4), $E(\mathbf{n})$ is a scalar function corresponding to the probability density function of $\mathbf{n}$ and Ω denotes the solid angle of the entire domain (4π steradians in 3-D and 2π rad in 2-D). Note that for spherical grains, $\mathbf{n}$ denotes also the unit vector from the centre of a grain to the centre of the next grain in contact with the former (things are different for ellipsoidal grains). We can also write the components of the contact fabric tensor as,

$$T^c_{ij} = \int_\Omega E(\mathbf{n})\,n_i n_j d\Omega. \tag{32}$$

In order to allow comparison with the electrical formation factor tensor, the void-based fabric tensor is also introduced here. Considering that a void cell is quantified by a void vector $v\cdot\mathbf{l}$ (where v is the void vector length and $\mathbf{l}$ is the unit vector along the void orientation, see Fig. 4), void cells can be tensorially studied. The void-based fabric tensor $\mathbf{T}^v$ defined by Li & Li (2009) is given as follows,

$$\mathbf{T}^v = E_0 \oint_\Omega \bar{v}(\mathbf{l})\,\mathbf{l} \otimes \mathbf{l} d\Omega, \tag{33}$$

where $\bar{v}(\mathbf{l})$ is the mean length of the void vectors along the given direction $\mathbf{l}$; E_0 is a normalization factor equals to 2π in 2-D space and 4π in 3-D space. The fabric tensor $\mathbf{T}^v$ is a statistical measure of the void spaces. Based on the directional distribution of the void vector length, $\mathbf{T}^v$ is believed to be a direct reflection of the void shape and its spatial arrangement.

For a fabric tensor $\mathbf{T}^*$ in 3-D space, the corresponding fabric anisotropy tensor $\mathbf{D}^*$ is defined as the deviatoric part of $\mathbf{T}^*$. We decompose now the fabric tensor into its isotropic and deviatoric parts D^*_{ij},

$$T^*_{ij} = \frac{1}{3}T^*_{kk}\delta_{ij} + D^*_{ij}, \tag{34}$$

$$D^*_{ij} = T^*_{ij} - \frac{1}{3}T^*_{kk}\delta_{ij} \tag{35}$$

where the superscript $*$ stands for c or$v$ (see above). The deviatoric part is different from zero in the anisotropic case and contains information regarding the departure of textural isotropy. For complex

symmetries, a fourth-order contact tensor is required (Cowin 1985). Normalizing the fabric anisotropy tensor yields

$$\mathbf{D} = \frac{\mathbf{T}^*}{\frac{1}{3}\mathrm{Tr}(\mathbf{T}^*)} - \mathbf{I}. \tag{36}$$

and $\mathbf{I}$ denotes the unit tensor. Note that the term $\mathrm{Tr}(\mathbf{T}^v)$ (Tr denotes the trace of the matrix) is a measure of the average void size that is closely correlated to the void ratio e (volume of void/volume of solid) or specific volume $v = 1 + e$ (Li & Dafalias 2015). The void ratio, related to the porosity ϕ by $e = \phi/(1-\phi)$, is often considered as a state variable to study the mechanical behaviour of soils. The fabric anisotropy tensor $\mathbf{D}$ is a unity-trace symmetrical second-rank tensor and it can be uniquely determined by scalar values such as the difference between the two principal components $\alpha_f = D_1 - D_3$. The parameter α_f is termed the anisotropy intensity factor. This factor quantifies the intensity of the anisotropy of the fabric of granular media (Oda 1982).

3.2 Electrical anisotropy tensor

The definition of the fabric anisotropy tensor $\mathbf{D}$ actually follows two criteria: (1) the definition is based only on the geometry of the pore space (and/or the solid phase) and the physical properties of the material are not involved; and (2) the definition is dimensionless and independent of the pore size. For instance, information on the 'average void size', $\mathrm{Tr}(\mathbf{T}^*)$, is used to normalize the fabric tensor (eq. 36). In Section 2, we define three conductivity-related tensors: σ_{ij}, F_{ij}, and H_{ij}, and we analyse below which is more appropriate to provide the electrical anisotropy tensor according to the criteria mentioned above. We can exclude σ_{ij} because it is related to the physical properties of the materials, that is, the fluid conductivity or specific surface conductance. In addition, the geometrical factor H_{ij} is also inappropriate for representing the electrical anisotropy tensor because it is defined on the internal surface of the sample rather than the pore space. The (conductivity) formation factor tensor $\mathbf{F}$ also cannot be regarded as the electrical anisotropy tensor either because it is still related to the porosity. However, we can define a new tensor that does not contain the 'average void size' information.

When considering Archie's equation (3), the formation factor F can be decomposed into an 'average void size' part ϕ and an 'average void shape' part m (e.g. see Norris *et al*. 1985),

$$\mathbf{F} = \phi^{\mathbf{m}} = \exp\left(\mathbf{m}\ln\phi\right). \tag{37}$$

where $\mathbf{F}$ is the conductivity formation factor tensor and $\mathbf{m}$ denotes the second-order symmetrical porosity exponent tensor. Note that the exponential of a matrix $\mathbf{A}$ ($\exp\mathbf{A}$) is a well-defined quantity given by,

$$\exp\left(\mathbf{A}\right) = \sum_{i=0}^{\infty} \frac{1}{i!}\mathbf{A}^i. \tag{38}$$

Eq. (37) corresponds to a generalized form of Archie's law, which can actually be obtained through the differential effective medium taken as upscaling approach for anisotropic granular porous media (see Mendelson & Cohen 1982, for details). It is also in agreement with experimental data. For instance in Fig. 2, we show the horizontal and vertical formation factors of compacted sands, which behave as a transversely isotropic material. Both the vertical horizontal and vertical formation factors can be connected to the connected porosity via Archie's law defining horizontal and vertical porosity exponents (m_{H} and m_{V}, respectively). According to eq. (37), we can define a second-order symmetric tensor $\mathbf{m}$ that only contains the 'average void shape' part of $\mathbf{F}$ by

$$\mathbf{m} = m_{ij}\,\mathbf{x}_i \otimes \mathbf{x}_j, \tag{39}$$

$$m_{ij} = \frac{\ln F_{ij}}{\ln\phi} = \log_{\phi} F_{ij}. \tag{40}$$

which is the base ϕ logarithm of F_{ij} (note that F_{ij} denotes the component of the formation conductivity tensor $\mathbf{F}$ and are therefore the reciprocal of the traditional formation factors).

We suggest that $\mathbf{m}$ is the suitable electrical anisotropy tensor because this tensor is fundamentally related to the texture of the porous material (Mendelson & Cohen 1982) in a way that is similar to the fabric anisotropy tensor $\mathbf{D}$. Like for $\mathbf{D}$, we can define the intensity of the anisotropy of the material from an electrical viewpoint using the difference between the two principal components of the tensor $\mathbf{m}$, that is $\alpha_e = m_1 - m_3$, where m_1 and m_3 denote the first and third eigenvalues of the tensors $\mathbf{m}$, respectively. As discussed above, numerical simulations could be a useful tool to identify and confirm the relation between $\mathbf{D}$ and $\mathbf{m}$ (or the anisotropy intensity factors α_e and α_f). This is done in the next two sections.

4 ELECTRICAL CONDUCTIVITY OF SYNTHETIC SAMPLES

4.1 Deformation of the synthetic core sample

The DEM software, 'Grain Flow Code in Three Dimensions' (PFC3D version 4.0, Itasca Company, USA) is used in this study to deform synthetic samples made of a collection of spherical grains. Spherical grains with different radii are used in the simulations (Fig. 5), and the grain radius follows a lognormal distribution with a mean value of 35.5 μm and a standard deviation of 0.1 (see Table 1 and Fig. 5b). The Hertz–Mindlin model is used to model the contact normal (using Hertz's theory) and tangential force (using Mindlin's no-slip model) displacement relations between the grains (e.g. Mindlin & Deresiewicz 1953). For DEM, the implementation of this model can be found in Di Renzo & Di Maio (2004) and Di Maio & Di Renzo (2005). The related parameters are summarized in Table 1. In order to account for the resultant effects of the interlocking occurring between real grains, the rolling resistance, that is, a pair of moments generated at the grain-to-grain contacts (Iwashita & Oda 1998), was used in our calculations. The two associated parameters are the rolling stiffness coefficient and the maximum rolling resistance coefficient, and their values are also shown in Table 1. Note that the values of some parameters in Table 1 are typical values calibrated for granular soils (see details in Kang *et al.* 2012; Wang *et al.* 2014; Zhang & Wang 2015). The loose synthetic sample used in the DEM simulation is shown in Fig. 5(a) with the grain size distribution shown in Fig. 5(b). Cubic synthetic samples (0.4 mm × 0.4 mm × 0.4 mm) can be extracted from the cylindrical synthetic samples at any stage of the deformation. There are used to compute the electrical conductivity tensor as discussed in the next section. These volumes contain approximately 150 grains and they correspond to a representative elementary volume (Fig. 4c).

4.2 Formulation of the problem

In this section, we present a numerical method that can calculate the directional conductivity of granular media so that it can be coupled with the DEM simulation for studying the fabric–electrical

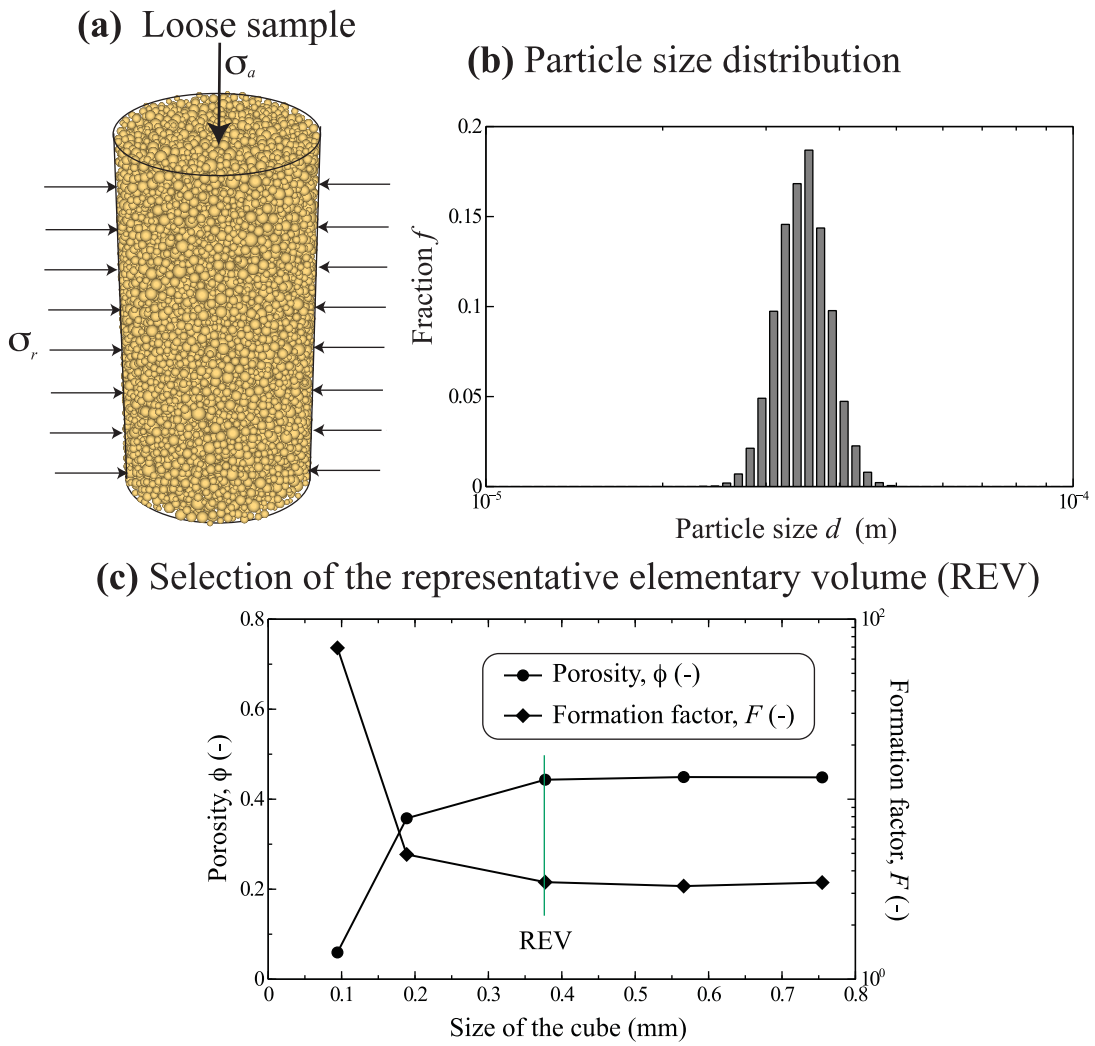

Figure 5. Sketch showing the loose synthetic sample used in this study (22 187 grains). (a) Loose sample used for the DEM simulation of a (drained) triaxial compression test and characterized by a starting porosity of 0.45. (b) Grain size distribution of the two synthetic samples (mean 35 μm). All the computations (for both the deformation and electrical conductivity) are conducted in 3-D. We start the deformation with samples that are perfectly isotropic. (c) Determination of the representative elementary volume (REV). Computations of the porosity and formation factor are made with cubes of different sizes extracted from the cylindrical core sample. The REV corresponds to cubes of 0.4^3 mm^3 with ∼150 grains.

anisotropy relation. We consider a cubic synthetic sample taken from an assembly of a granular synthetic sample at any shear stage in a DEM simulation. In the sample, we define the conductivity at position $\mathbf{r}$ as $\sigma(\mathbf{r})$. The current flow can be described by Laplace equation as

$$\nabla \cdot \mathbf{j}\ (\mathbf{r}) = 0 \tag{41}$$

or

$$-\nabla \cdot\ [\sigma\ (\mathbf{r}) \cdot \nabla \psi\ (\mathbf{r})] = 0 \tag{42}$$

where $\mathbf{j} = -\sigma(\mathbf{r}) \cdot \nabla\psi(\mathbf{r})$ (Ohm's law) denotes the local current density (position dependent) and ψ is the local electrical potential. The effective electrical conductivity of the synthetic sample can be determined by applying a uniform electrical field across the sample, which is fully saturated with a NaCl solution of conductivity σ_w. Therefore, the value of $\sigma(\mathbf{r})$ in eq. (42) is assigned as the fluid conductivity σ_w at positions within the pores of the synthetic sample. For positions occupied by solid grains, the conductivity $\sigma(\mathbf{r})$ is replaced by the specific surface conductivity σ_{ss}. For spherical grains, the specific surface conductivity has the following explicit form, $\sigma_{ss} = (2/a)[e\Gamma^d_{(+)} \cdot \beta_{(+)} \cdot (1 - f)]$, where a is the radius of the grain, $\Gamma^d_{(+)}$ is the surface site density of the adsorbed counterions in the diffuse layer and e is the elementary charge (1.6×10^{-19} C). Therefore, grains with different radii have different specific surface conductivities, small grains are more conductive than large grains.

To numerically solve eq. (42), the cubic synthetic sample is discretized in 3-D using a stacked-grid scheme and the grid in all three directions has the same interval d. The finite-difference representation of the Laplace equation is then solved in the synthetic sample domain. In this study, we modified for that purpose an industry standard finite-difference code (DC3D.F) developed at the National Institute of Standards and Technology (DC3D.F is available at http://ciks.cbt.nist.gov/garbocz/manual/node52.html) to realize the electrical conductivity calculations. For more details regarding this code, the interested readers can consult Garboczi (1998). The input to DC3D.F is a 3-D digital image. This 3-D image is converted into a real conductor network. The conjugate gradient method is used to solve this finite-difference representation of Laplace's equation (42) for the current density distribution. The calculated volume-averaged current density can then be used to determine

Table 1. Summary of the parameters used in the DEM simulation of drained triaxial compression tests and associated electrical conductivity calculations.

Properties	Values
Synthetic sample properties	
Mean grain radius	35 μm
Grain density	2650 kg m^{-3}
Initial porosity	0.38 (dense)
	0.45 (loose)
Grain number	24 992 (dense)
	22 187 (loose)
Contact model parameters	
Shear modulus	0.30 GPa
Poisson's ratio	0.20
Intergrain friction coefficient	1.50
Rolling stiffness coefficient	0.25 (dense)
Maximum rolling resistance coefficient	0.10 (dense)
Electrical parameters	
Pore water conductivity	0.005 S m^{-1}
Site density in diffuse layer	4.4×10^{15} m^{-2}
Mobility of ions in diffuse layer	11×10^{-8} $m^2V^{-1}s^{-1}$

the directional effective conductivity of the sample by considering Ohm's law.

In order to test the conductivity model, we perform electrical conductivity modeling with the same uncompacted synthetic sample (porosity 0.45) saturated at different pore water conductivities. The results are shown in Fig. 6. We see both the high salinity asymptotic behaviour for which the bulk conductivity dominates and the low salinity behaviour for which surface conductivity dominates the overall conductivity response. However, a closer inspection of the results indicates that the surface conductivity defined by eq. (10) is only a high salinity approximation (e.g. see Bussian 1983). Note that the surface conductivity at $\sigma_w = 5 \times 10^{-3}$ S m^{-1} (pore water conductivity at which the deformation experiments are numerically carried out) is about 8×10^{-5} S m^{-1}.

4.3 Conductivity change associated with isotropic consolidation

The first simulation we perform is to test the behaviour of the cementation exponent during isotropic consolidation of a granular media starting with a loose grain distribution and a porosity of 0.45. Fig. 7 shows a cross-section for the cubes used for the electrical conductivity simulations. We see clearly the densification of the granular material. Fig. 8 shows the consolidation curve for the porosity versus the isostatic confining stress. The core sample is more compressible initially, as expected, and strengthens further and further. In Figs 9 and 10, we plot the consolidation curve for the formation factor versus porosity and we compare the result with both experimental data (using sands and sandstones) and the differential effective medium theory with a cementation exponent of 1.5 (see Sen *et al*. 1981 for details of the derivation) and a percolation porosity of 0.005 (Fig. 9) and 0.014 (Fig. 10). The good agreement between the model and the synthetic and numerical data is very encouraging.

5 DRAINED TRIAXIAL COMPRESSIVE TEST

In this section, the proposed method is combined with DEM to simulate the mechanical and electrical conductivity responses of two granular media under a triaxial compression of a loose and dense

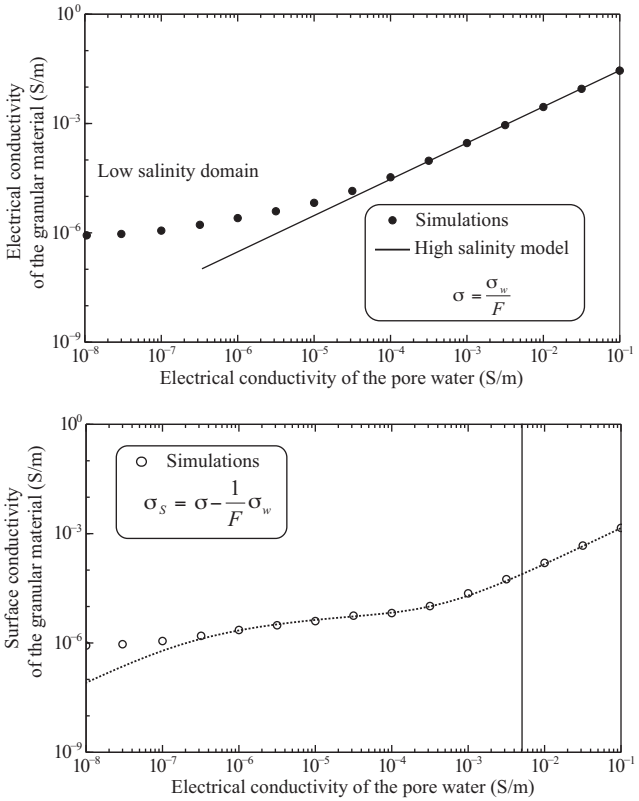

Figure 6. Electrical conductivity of the porous materials versus the pore water conductivity. The simulations are done with a cubic synthetic sample (porosity 0.45, dimensions 0.4 mm × 0.4 mm × 0.4 mm) saturated by electrolytes at different pore water conductivities. The upper figure shows the high and low salinity behaviours. The high salinity behaviour is used to determine the formation factor. However, if we determine the surface conductivity by subtracting the bulk conductivity σ_w/F from the synthetic sample conductivity, we see that the resulting surface conductivity is salinity dependent. This is due to the change of tortuosity associated with salinity. This behaviour is related to the changes in the current flow paths between high- and low-salinity behaviours as described for instance by Bernabé & Revil (1995). The dotted line corresponds to the differential effective medium theory (see discussion in Niu *et al.* 2016).

core synthetic samples. The loose material is characterized by a reference porosity of 0.45, while the dense material is characterized by a reference porosity of 0.38. Note that 0.38 is close to the porosity of a maximally random jammed sample (~0.36 for monospheres; see Torquato *et al*. 2000), while therefore 0.45 corresponds to a loose distribution of grains. Details of the simulations are presented below together with the numerical results. The relationship between the electrical and the fabric anisotropies of these two synthetic samples will be discussed at the end of this section.

5.1 Details of the simulations

The dense and loose synthetic samples are randomly generated for different stress–strain and volumetric responses. The triaxial compression tests will be assumed to be drained during shear since we do not compute the fluid pressure during the tests. The axial loading is applied under constant rate of strain. The stress $\sigma_1 = \sigma_a$ (axial stress) is applied in the vertical direction, while $\sigma_2 = \sigma_3 = \sigma_r$ (radial stress) are applied in the radial direction. These two synthetic samples are sheared with a confining pressure $P = 50$ kPa. We apply variable deviatoric stresses $\sigma_1 - \sigma_3$ until the axial strain ε_a

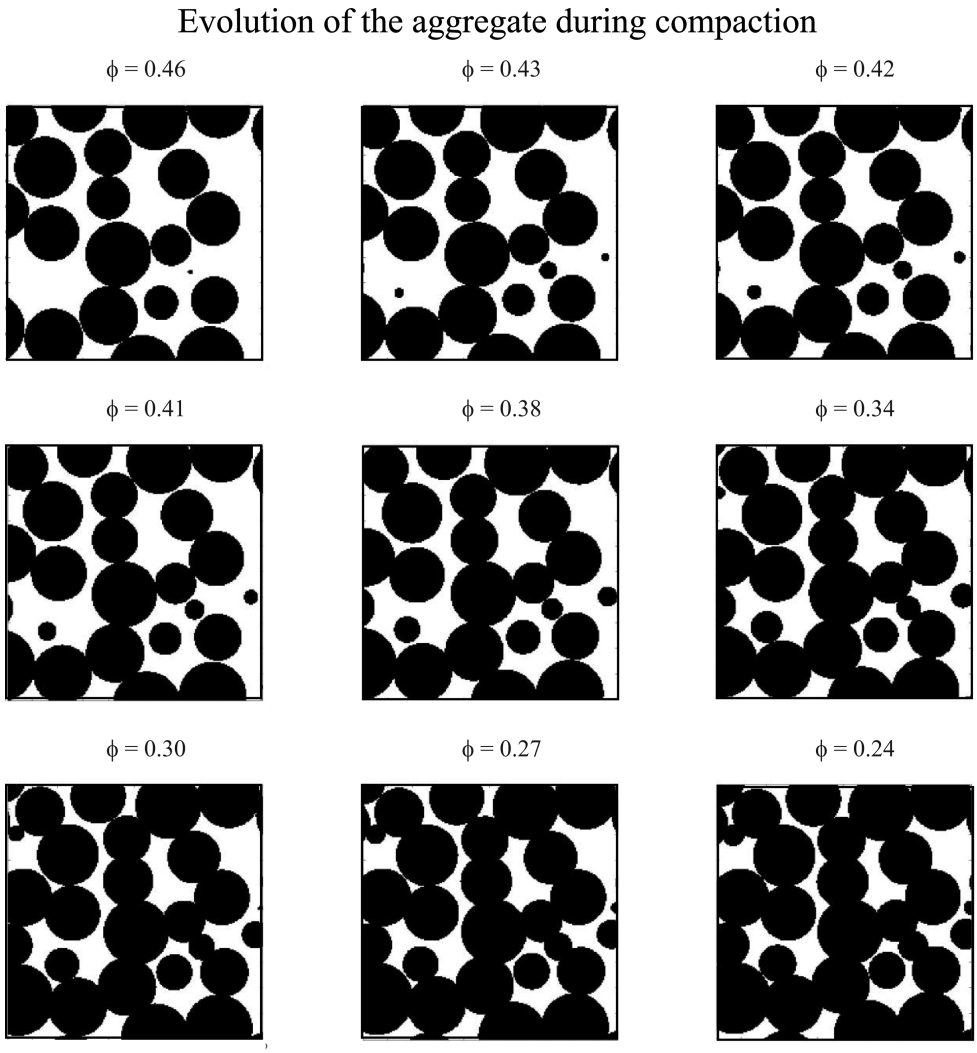

Figure 7. 2-D cross-plots of the 3-D cubes showing the evolution of the porosity and packing under the effect of the isostatic confining stress P. The mineral grains are in black and the pore space in white. Note that the computations of the electrical conductivity are done in 3-D.

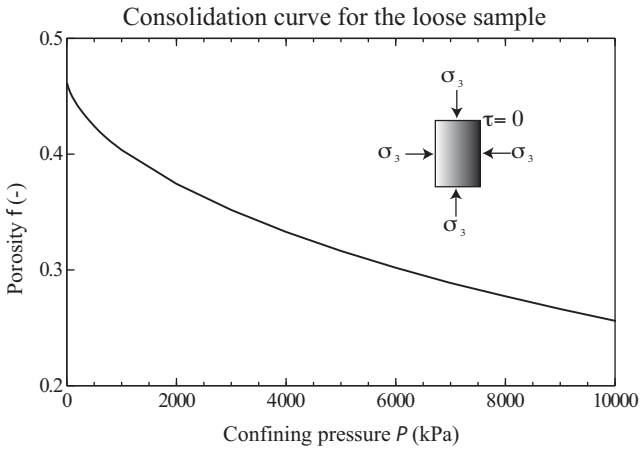

Figure 8. Porosity evolution during a consolidated-drained triaxial test. This isotropic consolidation curve is shown for the loose synthetic sample under the effect of the isostatic confining stress P. The quantity τ denotes the shear stress.

reaches 30 per cent and we monitor the changes in the volumetric strain, ε_V, the axial strain, ε_a, and the porosity, ϕ.

For these experiments, cubic synthetic samples (0.4 mm × 0.4 mm × 0.4 mm) are extracted from the cylindrical samples at distinct values of the axial strains with the increment $\Delta\varepsilon_a = 1$ per cent. We have demonstrated above (see Fig. 5c) that these cubic samples correspond to a good representative elementary volume of the whole material. Figs 11 and 12 show cross-sections of the cubic synthetic sample used for the electrical conductivity computations and the evolution of the aggregates during shearing. The directional electrical conductivity of the cubic samples is then calculated to monitor the evolution of the electrical conductivity of the material σ during shearing. The parameters related to the electrical calculations are also shown in Table 1. Note that the values of $\Gamma^d_{(+)}$ and $\beta_{(+)}$ are chosen to be very close to the values determined from experiments for silicates (Leroy *et al.* 2008; Revil 2012). We use 200^3 cells (i.e. $d = 0.2$ μm) to discretize the synthetic sample for all the calculations (approximately 8 million of cells).

5.2 Stress–strain and volumetric responses

The stress–strain and volumetric responses of the dense and loose synthetic samples are shown in Figs 13(a) and (b), respectively.

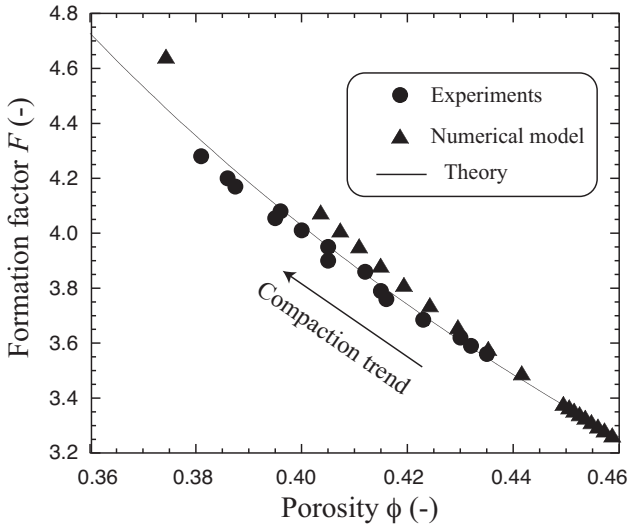

Figure 9. Evolution of the formation factor F with porosity during isotropic compaction. The plain line corresponds to the differential effective medium theory for spherical grains including a percolation threshold that is, $F = (\phi - \phi_p)^{-3/2}$ with $\phi_p = 0.005$. The data (filled circles) correspond to the Monterey sand compacted with a variety of methods (see details in Arulanandan & Kutter 1978). The numerical simulation (filled triangles) corresponds to the DEM model described in the main text.

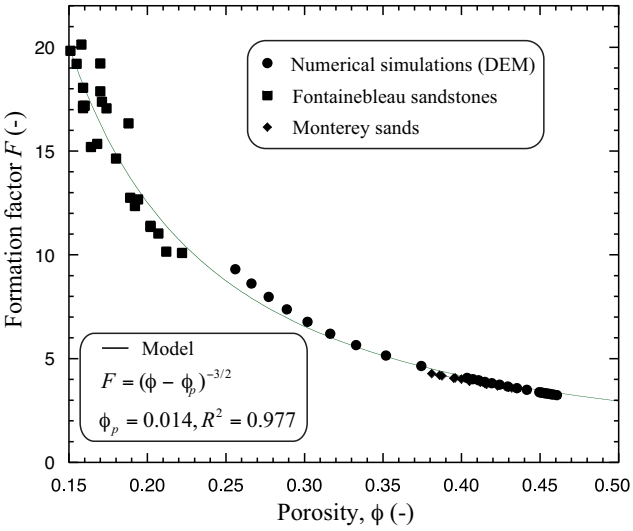

Figure 10. Evolution of the formation factor F with porosity during isotropic compaction (filled circles). Comparison with an extensive data set including the Fontainebleau sandstones (data from Revil *et al*. 2014, and sands (data from Arulanandan & Kutter 1978). The theory (plain line) corresponds to the differential effective medium theory for spherical grains including a percolation threshold, that is $F = (\phi - \phi_p)^{-3/2}$ with a percolation porosity $\phi_p = 0.014$. The value of R^2 indicates that the modified Archie's law works well for a broad range of porosity.

For both experiments, a uniform straining throughout the core samples (called the critical state) has been reached (Schofield & Wroth 1968). The stress–strain and volumetric responses are qualitatively representative of typical granular materials showing either a peak followed by a plateau or just a plateau in the deviatoric stress versus axial strain curve. The dense synthetic sample experiences a hardening–softening process. Correspondingly, the volumetric response first contracts and then dilates. In contrast, the synthetic loose sample continuously hardens and contracts until reaching the critical state. Note that both samples have reached the critical state at the end of the numerical experiments (steady-state shearing conditions shown by the plateau) when $\varepsilon_a >$ ~25 per cent. The behaviours are exactly those shown in the literature for dense and loose sands (Kolymbas & Wu 1990; Schanz & Vermeer 1996; Pietruszczak 2010).

5.3 Electrical conductivity evolutions

The directional bulk conductivity of the synthetic sample (x-, y- and z-directions) at different axial strains is shown in Figs 14(a) and (b) for the loose and dense synthetic samples, respectively. Note that the deviatoric stress is applied along the z-direction and the (x, y)-plane is perpendicular to the z-direction. As shown in Fig. 14, the bulk conductivity σ_b of these two synthetic samples shows similar trends with the volumetric strain. This is understandable because σ_b is controlled by the formation factor, and thus, by the porosity ϕ of the sample. When $\varepsilon_a >$ ~25 per cent, it seems that the bulk conductivity in all directions stays unchanged. It is also found that the σ_b responses in the x(y)- and z-directions start to deviate from each other after the deviatoric stress is applied, although their initial values are the same. It is noted that σ_b in the z-direction is slightly larger than that in the x(y)-direction during shearing, indicating the occurrence of shear-induced electrical anisotropy. Considering that the porosity is the same in all directions, it appears that the shear-induced electrical anisotropy is mainly from the anisotropy in the cementation factor m, as discussed in Section 3.2.

The directional surface conductivity σ_s is shown in Figs 15(a) and (b) for the loose and dense synthetic samples, respectively. Note that the value is consistent with what is shown in Fig. 6 at the salinity of the pore water used for the simulation of the mechanical test. For both samples, it seems σ_s maintains unchanged during the entire shearing process, indicating that there is no influence from the shearing. This can be explained by the constant specific surface conductivity of the synthetic sample during shearing, which controls the surface conductivity of the synthetic sample. Differing from the bulk conductivity, no anisotropy is found in the surface conductivity σ_s for both samples. This shows that the geometric factor H_{ij} is almost the same for all directions, implying that the tensor H_{ij} is not a good indicator for the electrical anisotropy (this is consistent with our theoretical analysis shown above). According to eq. (30), it means that the local electrical field near the mineral–fluid interface is not significantly affected by shearing.

5.4 Relation between fabric and electrical anisotropy factors

We calculated the electrical anisotropy intensity factors α_e at different axial strains from the directional conductivity, fluid conductivity and porosity of the samples, and the results are shown in Fig. 16. It is clear that the shear strain induces a clear anisotropy in the electrical conductivity of both loose and dense granular media. For the loose synthetic sample, it is shown that α_e increases gradually as ε_a increases and, after reaching the critical state, α_e maintains unchanged. The response of the dense sample is distinct from the loose synthetic sample. At a small axial strain (~5 per cent), α_e reaches its maximum value. After the peak, α_e starts to decrease as the shearing proceeds to the critical state.

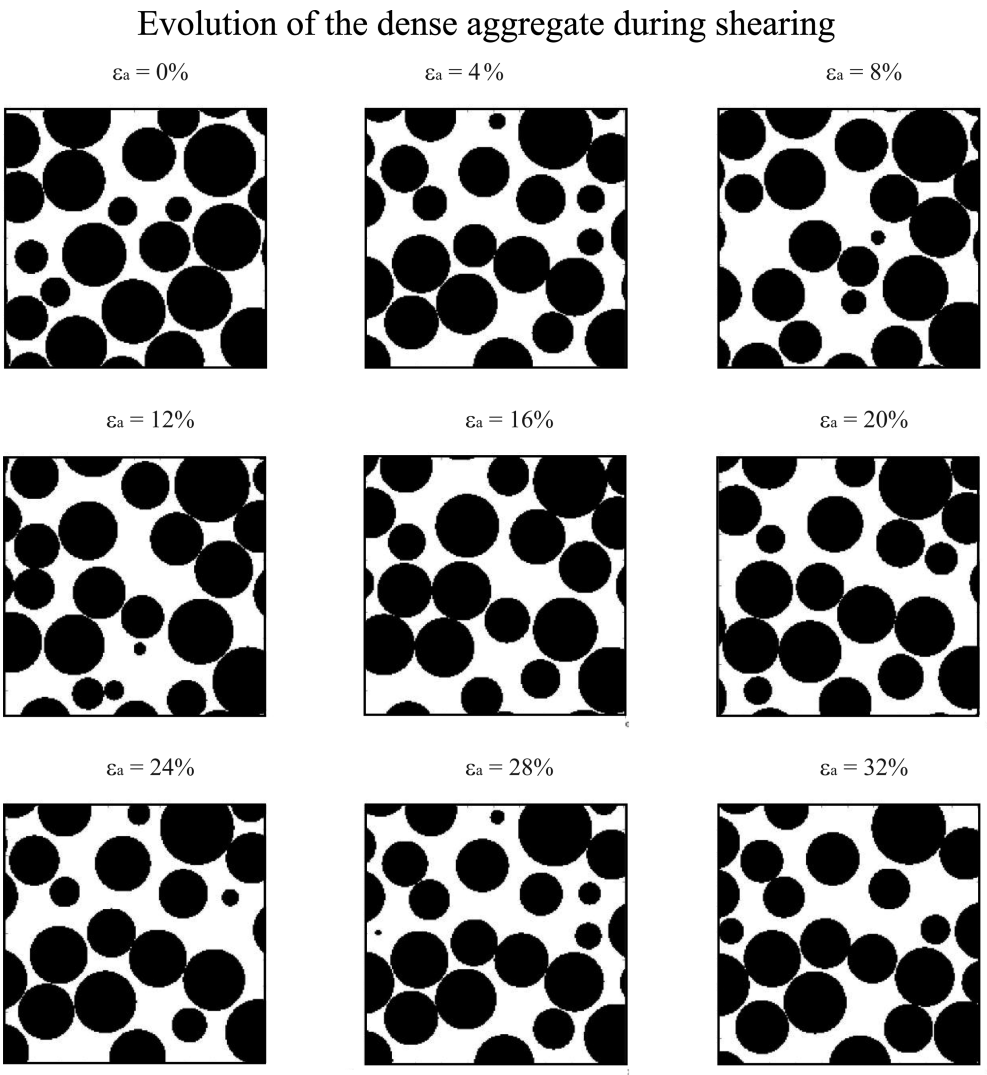

Figure 11. 2-D cross-plots of the 3-D cubes (computations are done in 3-D) showing the evolution of the packing of the dense synthetic sample when the material is submitted to shearing. The mineral grains are in black and the pore space is represented in white. The plots are shown for different values of the axial strains ε_a. Note the evolution of the porosity of the material. This sample experiences a hardening–softening process during the triaxial compression test.

We now explore the correlation between fabric and electrical anisotropies based on the numerical results. Among the three kinds of the aforementioned fabric tensors, it is straightforward to calculate the void-based fabric tensor $\mathbf{T}^v$ which is defined on the void space, as is similar to the electrical fabric tensor $\mathbf{F}$. However, to calculate $\mathbf{T}^v$, few mature methods for 3-D void cell partition are currently available. Also, since the contact normal-based fabric tensor $\mathbf{T}^c$ is positively correlated to $\mathbf{T}^v$ (Theocharis *et al.* 2014; Fu & Dafalias 2015), for the sake of convenience, here $\mathbf{T}^c$ is used instead to characterize the fabric for the two synthetic samples. For the specified cases considered, the contact normal-based fabric is transformed from the continuous form to the discretized form as (Oda 1982)

$$\mathbf{T}^c = \frac{1}{N_c} \sum_{c=1}^{N_c} \mathbf{n}^c \otimes \mathbf{n}^c \tag{43}$$

where N_c is the total number of contact normal vectors $\mathbf{n}^c$ in the domain, and the superscript c denotes the cth contact in the domain. Note that the fabric anisotropy tensor $\mathbf{D}$ is calculated following eq. (36). The calculated fabric anisotropy intensity factor α_f is plotted in Fig. 16 for comparison. The fabric and electrical anisotropies have similar trends during shearing for both dense and loose synthetic samples. The practical implication of this finding is important, and it proves that the electrical measurement can be used to determine the fabric anisotropy of granular media. Conversely, this correlation provides a physical picture to the evolution of the cementation exponent during shearing of granular media.

Fig. 16 confirms the correlation between the fabric and the electrical anisotropy factors for both dense and loose samples. In order to test whether these two correlations are the same, in Fig. 17, we cross-plot the electrical anisotropy factor α_e and the fabric anisotropy factor α_f at different axial strains for both samples. We note that the α_e–α_f correlation is slightly different for the dense and loose samples, but in general, both synthetic samples follow the same linear trend with $R^2 = 0.92$. This implies that the electrical–fabric anisotropy relation for a granular material might be unique and is independent of the stress and strain states of the material. Further studies are still needed to test whether this linear correlation holds for core samples with different porosities, intergrain frictions and grain shape and sizes. The slight difference in

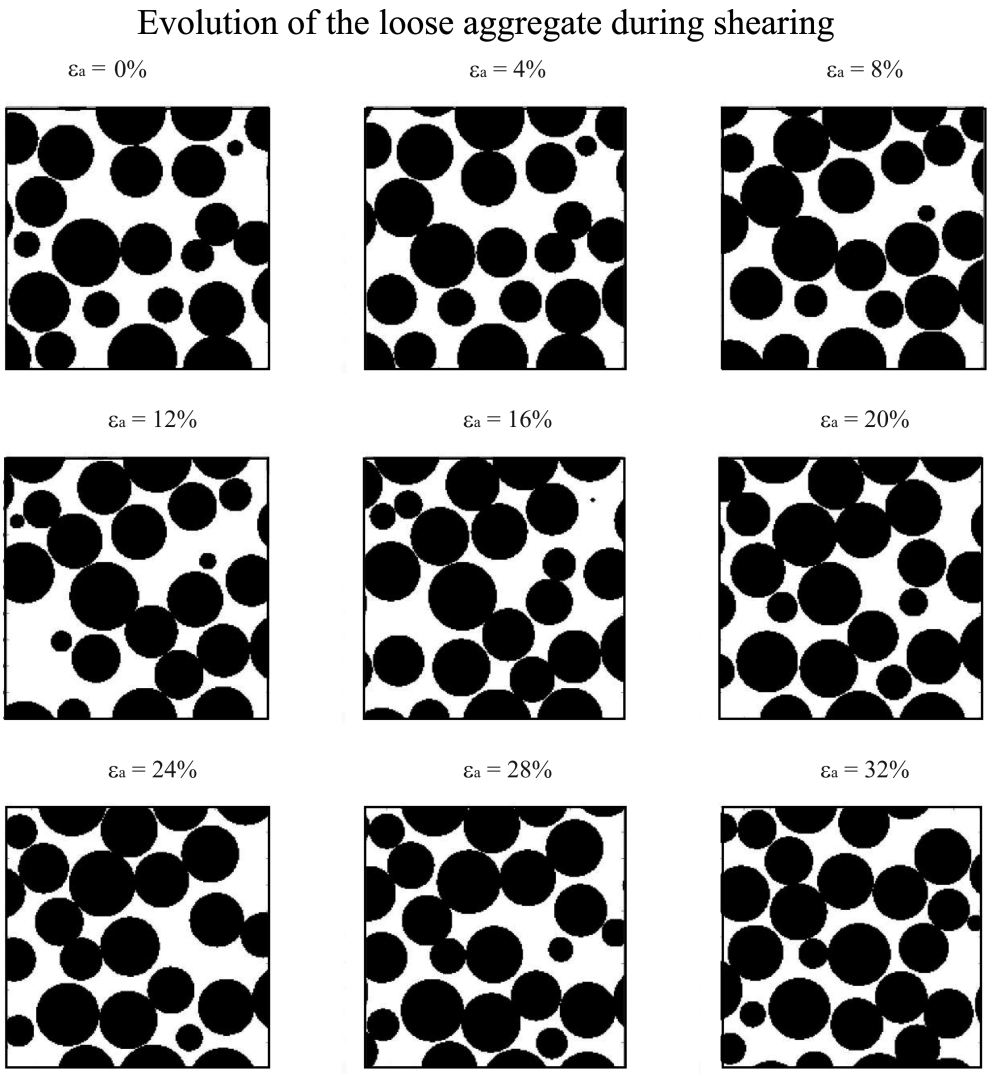

Figure 12. 2-D cross-plots of the 3-D cubes (computations are done in 3-D) showing the evolution of the packing of the loose synthetic sample when this material is submitted to shearing. The mineral grains are in black and the pore space is represented in white. The plots are shown for different values of the axial strains ε_a. Note the densification of the material. This sample continuously hardens during shearing and therefore contracts until reaching the critical state for an axial strain> 24 per cent.

α_e–α_f correlation between loose and dense samples might be due to the fact that the deformation in triaxial tests is localized (Higo *et al*. 2013), and therefore, the calculated α_f is influenced by the sample location.

Finally, since the fabric tensor can be used to characterize the linear poroelastic behaviour of Earth materials (e.g. Cowin 2004), the present relationship between electrical and fabric anisotropies opens a path in a unified framework between electrical conductivity and seismic velocity in isotropic an anisotropic granular media. This will be developed in a future work.

6 CONCLUSIONS

We have defined an electrical anisotropy tensor that is analogous to the fabric anisotropy tensor used in rock mechanics. This electrical anisotropy tensor is based only on the geometry of the pore space and thus on physical properties of the material are involved in the definition. Similar to the fabric anisotropy, the electrical anisotropy tensor is dimensionless and independent of the pore size. The electrical anisotropy tensor can be used to quantify the anisotropy in granular media like soils from an electrical viewpoint. We have shown that we are still not able to obtain a theoretical relation between the electrical and fabric anisotropies, although the correlation between them seems apparent. To identify and confirm the relationship, we have presented a finite-difference-based numerical method for the calculation of the electrical conductivity of granular media. The method is easily coupled with the DEM to study the electrical and mechanical properties and the anisotropy of granular media.

The proposed method has been used to simulate the directional electrical conductivity evolution of dense and loose synthetic samples subjected to triaxial compression. The results show that the shear strain has a significant effect on the electrical conductivity of granular media. The bulk conductivity exhibits similar trends to the volumetric stain for both loose and dense samples. Significant anisotropy in the bulk conductivity is found in directions parallel and perpendicular to the deviatoric stress. This anisotropy increases gradually with axial strain for the loose synthetic sample; for the dense synthetic sample, it peaks at a low axial strain and then decreases continuously until reaching a steady value.

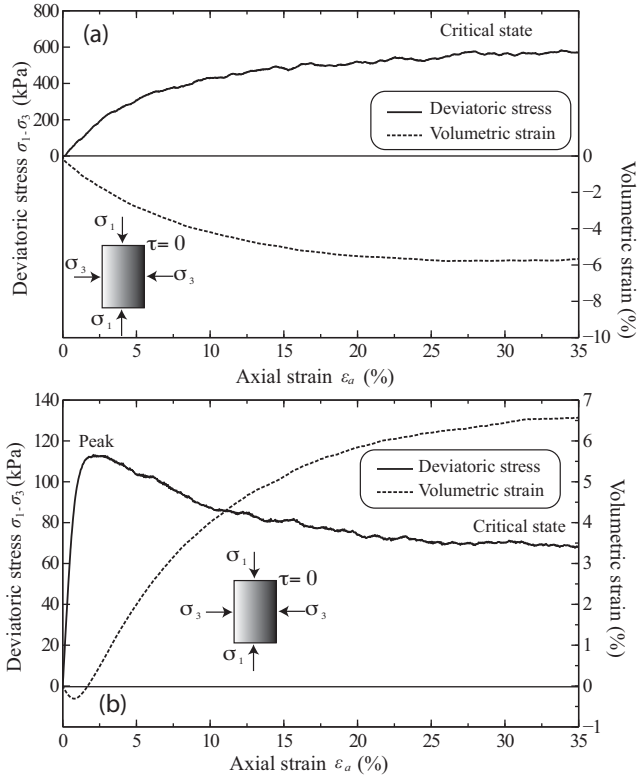

Figure 13. The stress–strain responses of the two synthetic samples under triaxial compression as a function of the axial strain. (a) Deviatoric and volumetric strain as a function of the axial strain for the loose synthetic sample. For this numerical experiment, the deviatoric stress reaches a plateau with no reduction in strength with continued straining. (b) Deviatoric and volumetric strain as a function of the axial strain for the dense synthetic sample for which we see a pronounced peak in the deviatoric stress versus axial strain at failure with a clear drop in strength under continued straining. The quantity τ denotes the shear stress.

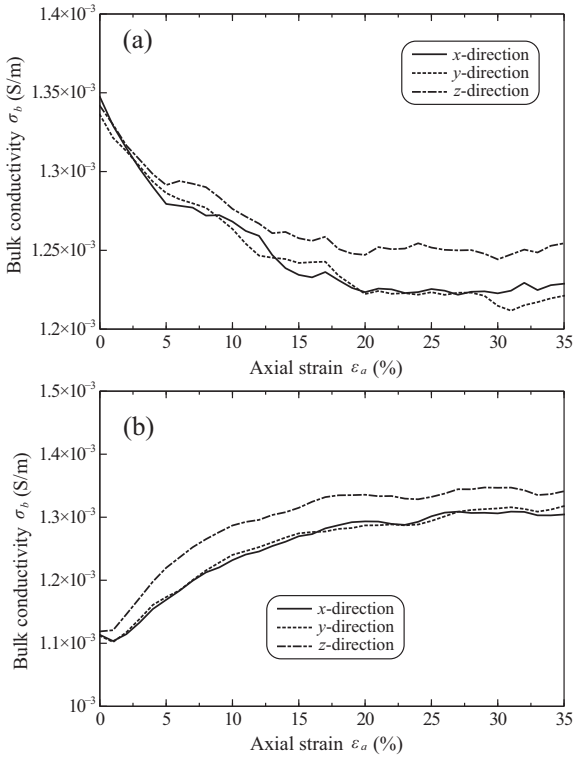

Figure 14. Evolution of the directional bulk conductivity $\sigma_b = \sigma_w/F$ during the drained triaxial compression tests as a function of the axial strain. (a) Loose synthetic sample. (b) Dense synthetic sample.

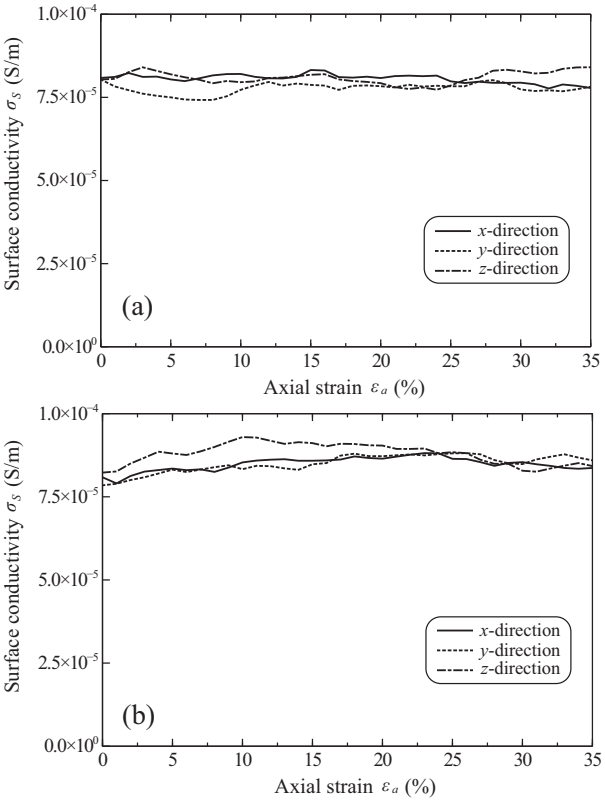

Figure 15. Evolution of the directional surface conductivity during shearing as a function of the axial strain. (a) Loose synthetic sample. (b) Dense synthetic sample. We see that the surface conductivity is not strongly affected by the deformation of the core samples.

However, shear-induced variations and anisotropy was not found in the surface conductivity of both samples. This is mainly because the surface conduction is controlled by the specific surface conductance, and thus, the fluid–mineral interface, which does not change during shearing.

The comparison between the calculated fabric and electrical anisotropies shows that the intensity of these two anisotropies has similar trends during shearing for both the dense and loose synthetic samples. It also shows that a linear relationship exists between the fabric and electrical anisotropies, and it seems the relationship is independent of the shear strain and the initial density of the samples. The practical implication of this finding is important, and it shows the potential of electrical conductivity measurement as a powerful tool for the determination of the fabric anisotropy in granular media. Further studies are suggested to study the influence of other properties of porous media (such as porosity, intergrain friction and grain shapes and sizes) on the linear correlation between the fabric and electrical anisotropies.

ACKNOWLEDGEMENTS

This research was partially supported by the Hong Kong Research Grants Council (project no. T22-603/15-N) and Hong Kong PhD Fellowship Scheme (HKPFS). We thank the editor, two anonymous

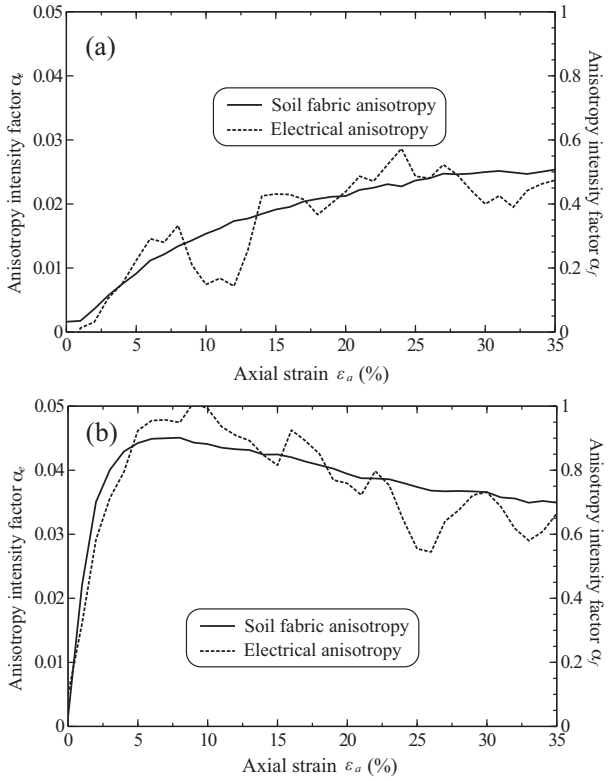

Figure 16. Evolution of the fabric and electrical anisotropies during shearing. (a) Loose synthetic sample. (b) Dense synthetic sample. We see that the evolution of the electrical anisotropy intensity factor mimics the trend displayed by the fabric anisotropy intensity factor during deformation.

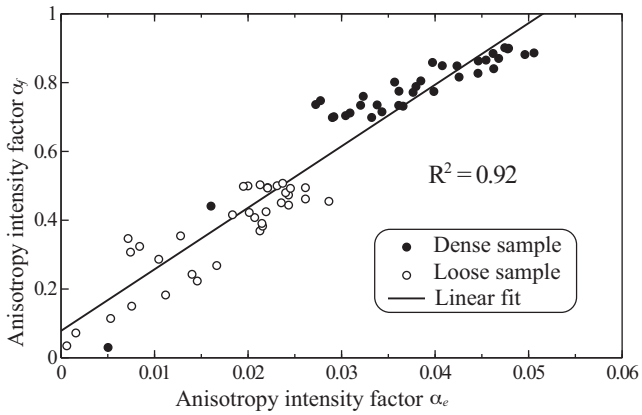

Figure 17. Correlation between fabric (α_f) anisotropy and electrical (α_e) anisotropy for the loose and dense synthetic samples at different strain states. A total of 68 synthetic numerical experiments are used here displaying a unique linear relationship between the two quantities.

referees and Dr Vladimir Puzyrev for their very useful comments on our manuscript and their time.

REFERENCES

Abu-Hassanein, Z., Benson, C. & Blotz, L., 1996. Electrical resistivity of compacted clays, *J. Geotech. Eng.,* **122**(5), 397–406.

Anandarajah, A., 1994. A constitutive model for granular materials based on associated flow rule, soils and foundations, *Japan. Soc. Soil Mech. Found. Eng.,* **34**(3), 81–98.

Anandarajah, A., Kuganenthira, N. & Zhao, D., 1996. Variation of fabric anisotropy of kaolinite in triaxial loading, *J. Geotech. Eng.—ASCE,* **122**(8), 633–640.

Andò, E., Hall, S.A., Viggiani, G., Desrues, J. & Bésuelle, P., 2012. Experimental micromechanics: grain-scale observation of sand deformation, *Géotech. Lett.,* **2,** 107–112.

Archie, G.E., 1942. The electrical resistivity log as an aid in determining some reservoir characteristics, *Pet. Trans. AIME,* **146,** 54–62.

Arulanandan, K. & Kutter, B., 1978. A directional structure index related to sand liquefaction, in *From Volume I of Earthquake Engineering and Soil Dynamics—Proceedings of the ASCE Geotechnical Engineering Division Specialty Conference*, June 19–21, 1978, Pasadena, California.

Arulanandan, K., Harvey, S.J. & Chak, J.S., 1981. Electrical characterization of soil for in-situ measurement of liquefaction potential (April 26, 1981), in *International Conferences on Recent Advances in Geotechnical Earthquake Engineering and Soil Dynamics,* Paper 17. http://scholarsmine.mst.edu/icrageesd/01icrageesd/session08/17.

Bernabé, Y. & Revil, A., 1995. Pore-scale heterogeneity, energy dissipation and the transport properties of rocks, *Geophys. Res. Lett.,* **22**(12), 1529–1552.

Berkowitz, B. & Ewing, R., 1998. Percolation theory and network modeling applications in soil physics, *Surv. Geophys.,* **19**(1), 23–72.

Börner, F.D., 1992. Complex conductivity measurements of reservoir properties, in *Proceedings of the Third European Core Analysis Symposium*, pp. 359–386.

Bryson, L., 2005. Evaluation of geotechnical parameters using electrical resistivity measurements, *Earthq. Eng. Soil Dyn.,* 1–12, doi:10.1061/40779(158)10.

Bussian, A., 1983. Electrical conductance in a porous medium, *Geophysics,* **48,** 1258–1268.

Cambou, B., Dubujet, P. & Nouguier-Lehon, C., 2004. Anisotropy in granular materials at different scales, *Mech. Mater.,* **36**(12), 1185–1194.

Carroll, S.A., Maxwell, R.S., Bourcier, W., Martin, S. & Hulsey, S., 2002. Evaluation of silica-water surface chemistry using NMR spectroscopy, *Geochim. Cosmochim. Acta,* **66**(6), 913–926.

Collins, I.F. & Muhunthan, B., 2003. On the relationship between stress–dilatancy, anisotropy, and plastic dissipation for granular materials, *Geotechnique,* **53**(7), 611–618.

Cowin, S.C., 1985. Relationship between the elasticity tensor and the fabric tensor, *Mech. Mater.,* **4**(2), 137–147.

Cowin, S.C., 2004. Anisotropic poroelasticity: fabric tensor formulation, *Mech. Mater.,* **36,** 665–677.

Di Maio, F & Di Renzo, A., 2005. Modelling particle contacts in distinct element simulations: linear and non-linear approach, *Chem. Eng. Res. Des.,* **83**(11), 1287–1297.

Di Renzo, A. & Di Maio, F.P., 2004. Comparison of contact-force models for the simulation of collisions in DEM-based granular flow codes, *Chem. Eng. Sci.,* **59**(3), 525–541.

Dvorkin, J., Derzhi, N., Diaz, E. & Fang, Q., 2011. Relevance of computational rock physics, *Geophysics,* **76**(5), E141–E153.

Friedman, S.P., 2005. Soil properties influencing apparent electrical conductivity: a review, *Comput. Electron. Agric.,* **46**(1–3), 45–70.

Friedman, S.P. & Jones, S.B., 2001. Measurement and approximate critical path analysis of the pore-scale-induced anisotropy factor of an unsaturated porous medium, *Water Resour. Res.,* **37**(12), 2929–2942.

Fu, P. & Dafalias, Y.F., 2015. Relationship between void- and contact normal-based fabric tensors for 2D idealized granular materials. *Int. J. Solids Struct.,* **63,** 68–81.

Gao, Z., Zhao, J. & Yao, Y., 2010. A generalized anisotropic failure criterion for geomaterials, *Int. J. Solids Struct.,* **47**(22–23), 3166–3185.

Garboczi, E.J., 1998. *Finite Element and Finite Difference Programs for Computing the Linear Electric and Elastic Properties of Digital Images of Random Materials*, Building and Fire Research Laboratory, National Institute of Standards and Technology.

Ghedia, R. & O'Sullivan, C., 2012. Quantifying void fabric using a scan-line approach, *Comput. Geotech.,* **41,** 1–12.

Guo, N. & Zhao, J., 2013. The signature of shear-induced anisotropy in granular media, *Comput. Geotech.,* **47,** 1–15.

Haas, A.K., Revil, A., Karaoulis, M., Frash, L., Hampton, J., Gutierrez, M. & Mooney, M., 2013. Electrical potential source localization reveals a borehole leak during hydraulic fracturing, *Geophysics,* **78**(**2**) D93–D113.

Hausenblas, M., 1995. Stress dependence of the cementation exponent, in *1995 SCA Conference,* Paper number 9518, p. 10.

Higo, Y., Oka, F., Sato, T., Matsushima, Y. & Kimoto, S., 2013. Investigation of localized deformation in partially saturated sand under triaxial compression using microfocus X-ray CT with digital image correlation, *Soils Found.,* **53**(2), 181–198.

Iwashita, K. & Oda, M., 1998. Rolling resistance at contacts in simulation of shear band development by DEM, *J. Eng. Mech.,* **124**(3), 285–292.

Jardani, A., Revil, A. & Dupont, J.P., 2013. Stochastic joint inversion of hydrogeophysical data for salt tracer test monitoring and hydraulic conductivity imaging, *Adv. Water Res.,* **52,** 62–77.

Johnson, D.L. & Sen, P.N., 1988. Dependence of the conductivity of a porous medium on electrolyte conductivity, *Phys. Rev. B,* **37**(7), 3502–3510.

Kang, D.H., Yun, T.S., Lau, Y.M. & Wang, Y.H., 2012. DEM simulation on soil creep and associated evolution of pore characteristics, *Comput. Geotech.,* **39,** 98–106.

Kim, F.H., Penumadu, D., Gregor, J., Kardjilov, N. & Manke, I., 2013. High-resolution neutron and X-ray imaging of granular materials, *J. Geotech. Geoenviron. Eng.,* **139**(5), 715–723.

Koch, K., Revil, A. & Holliger, K., 2012. Relating the permeability of quartz sands to their grain size and spectral induced polarization characteristics, *Geophys. J. Int.,* **190,** 230–242.

Kolymbas, D. & Wu, W., 1990. Recent results of triaxial tests with granular materials, *Powder Technol.,* **60,** 99–119.

Kuganenthira, N., Zhao, D. & Anandarajah, A., 1996. Measurement of fabric anisotropy in triaxial shearing, *Geotechnique,* **46**(4), 657–670.

Leroy, P. & Revil, A., 2009. A mechanistic model for the spectral induced polarization of clay materials, *J. geophys. Res.,* **114,** B10202, doi:10.1029/2008JB006114.

Leroy, P., Revil, A., Kemna, A., Cosenza, P. & Ghorbani, A., 2008. Complex conductivity of water-saturated packs of glass beads, *J. Colloid Interface Sci.,* **321**(1), 103–117.

Li, X. & Dafalias, Y., 2012. Anisotropic critical state theory: role of fabric, *J. Eng. Mech.,* **138**(3), 263–275.

Li, X. & Li, X.-S., 2009. Micro-macro quantification of the internal structure of granular materials, *J. Eng. Mech.,* **135**(7), 641–656.

Li, X.S. & Dafalias, Y.F., 2015. Dissipation consistent fabric tensor definition from DEM to continuum for granular media, *J. Mech. Phys. Solids,* **78,** 141–153.

Mahardika, H., Revil, A. & Jardani, A., 2012. Waveform joint inversion of seismograms and electrograms for moment tensor characterization of fracking events, *Geophysics,* **77**(5), ID23–ID39.

Mendelson, K.S. & Cohen, M.H., 1982. The effect of grain anisotropy on the electrical properties of sedimentary rocks, *Geophysics,* **47,** 257–263.

Mindlin, R.D. & Deresiewicz, H., 1953. Elastic spheres in contact under varying oblique forces, *SME J. appl. Mech.,* **20,** 327–344.

Mirzababaei, M. & Yasrobi, S., 2007. Assessment of clay soil fabric using scanning electron microscope (SEM), in *Proceedings of the Sri Lankan Geotechnical Society's 1st International Conference on Soil and Rock Engineering,* Sri Lanka.

Niu, Q., Prasad, M., Revil, A. & Saidian, M., 2016. Textural control on the quadrature conductivity of porous media, *Geophysics,* **81**(5), E297–E309.

Norris, A.N., Sheng, P. & Callegari, A.J., 1985. Effective-medium theories for two-phase dielectric media, *J. Appl. Phys.,* **57**(6), 1990–1996.

O'konski, C.T., 1960. Electric properties of macromolecules. V. Theory of ionic polarization in polyelectrolytes, *J. Phys. Chem.,* **64**(5), 605–619.

Oda, M., 1972. Initial fabrics and their relations to mechanical properties of granular material, *Soils Found.,* **12,** 17–36.

Oda, M., 1976. *Fabrics and Their Effects on the Deformation Behaviors of Sand,* Department of Foundation Engineering, Saitama University.

Oda, M., 1982. Fabric tensor for discontinuous geological materials, *Soils Found.,* **22**(4), 96–108.

Pietruszczak, S., 2010. *Fundamentals of Plasticity in Geomechanics,* CRC Press.

Revil, A., 2012. Spectral induced polarization of shaly sands: influence of the electrical double layer, *Water Resour. Res.,* **48**(2), W02517, doi:10.1029/2011WR011260.

Revil, A., 2013a. On charge accumulations in heterogeneous porous materials under the influence of an electrical field, *Geophysics,* **78**(4), D271–D291.

Revil, A., 2013b. Effective conductivity and permittivity of unsaturated porous materials in the frequency range 1 mHz–1 GHz, *Water Resour. Res.,* **49**(1), 306–327.

Revil, A. & Cathles, L.M., 1999. Permeability of shaly sands, *Water Resour. Res.,* **35**(3), 651–662.

Revil, A. & Florsch, N., 2010. Determination of permeability from spectral induced polarization in granular media, *Geophys. J. Int.,* **181**(3), 1480–1498.

Revil, A. & Glover, P.W.J., 1997. Theory of ionic surface electrical conduction in porous media, *Phys. Rev. B,* **55**(3), 1757–1773.

Revil, A., Woodruff, W., Torres-Verdín, C. & Prasad, M., 2013. Complex conductivity tensor of anisotropic hydrocarbon-bearing shales and mudrocks, *Geophysics,* **78**(6), D403–D418.

Revil, A., Kessouri, P. & Torres-Verdín, C., 2014. Electrical conductivity, induced polarization, and permeability of the Fontainebleau sandstone, *Geophysics,* **79**(5), D301–D318.

Revil, A., Mao, D., Haas, A.K., Karaoulis, M. & Frash, L., 2015. Passive electrical monitoring and localization of leakages in wells using electrography, *J. Hydrol.,* **521,** 286–301.

Rinaldi, V. & Cuestas, G., 2002. Ohmic conductivity of a compacted silty clay, *J. Geotech. Geoenviron. Eng.,* **128**(10), 824–835.

Rothenburg, L. & Bathurst, R.J., 1989. Analytical study of induced anisotropy in idealized granular materials, *Geotechnique,* **39**(4), 601–614.

Schanz, T. & Vermeer, P.A., 1996. Angles of friction and dilatancy of sand, *Géotechnique,* **46,** 145–151.

Schofield, A.W. & Wroth, C.P., 1968. *Critical State Soil Mechanics,* McGraw-Hill.

Scholtès, L. & Donzé, F.V., 2012. Modelling progressive failure of fractured rock masses using a 3D discrete element method, *Int. J. Rock Mech. Min. Sci.,* **52,** 18–30.

Scholtès, L., Hicher, P.Y., Nicot, F., Chareyre, B. & Darve, F., 2009. On the capillary stress tensor in wet granular materials, *Int. J. Numer. Anal. Methods Geomech.,* **33,** 1289–1313.

Seladji, S., Cosenza, P., Tabbagh, A., Ranger, J. & Richard, G., 2010. The effect of compaction on soil electrical resistivity: a laboratory investigation, *Eur. J. Soil Sci.,* **61**(6), 1043–1055.

Sen, P.N., Scala, C. & Cohen, M.H., 1981. A self-similar model for sedimentary rocks with application to the dielectric constant of fused glass beads, *Geophysics,* **46**(5), 781–795.

Shabro, V., Kelly, S., Torres-Verdín, C., Sepehrnoori, K. & Revil, A., 2014. Pore-scale modeling of electrical resistivity and permeability in FIB-SEM images of organic mudrock, *Geophysics,* **79**(5), D289–D299.

Shainberg, I., Rhoades, J.D. & Prather, R.J., 1980. Effect of ESP, cation exchange capacity, and soil solution concentration on soil electrical conductivity, *Soil Sci. Soc. Am. J.,* **44,** 469–473.

Shilov, V.N., Delgado, A.V., Gonzalez-Caballero, F. & Grosse, C., 2001. Thin double layer theory of the wide-frequency range dielectric dispersion of suspensions of non-conducting spherical particles including surface conductivity of the stagnant layer, *Colloids Surf. A: Physicochem. Eng. Aspect,* **192,** 253–265.

Theocharis, A., Vairaktaris, E., Fu, P. & Dafalias, Y.F., 2014. Comparison of fabric tensors for granular materials, in *Geomechanics from Micro to Macro*, pp. 153–158, CRC Press.

Torquato, S., Truskett, T.M. & Debenedetti, P.G., 2000. Is random close packing of spheres well defined, *Phys. Rev. Lett.,* **84**(10), 2064–2067.

Torskaya, T., Shabro, V., Torres-Verdín, C., Salazar-Tio, R. & Revil, A., 2014. Grain shape effects on permeability, formation factor, and capillary

pressure curve from pore-scale modeling, *Transp. Porous Media,* **102,** 71–86.

Van Olphen, H. & Waxman, M., 1958. Surface conductance of sodium bentonite in water, in *Proceedings of the Fifth National Conference, Clays and Clay Minerals*, Vol. 5, pp. 61–80, National Academy of Sciences and National Research Council.

Viggiani, G., Lenoir, N., Bésuelle, P., Di Michiel, M., Marello, S., Desrues, J. & Kretzschmer, M., 2004. X-ray microtomography for studying localized deformation in fine-grained geomaterials under triaxial compression, *C. R. Méc.,* **332** (10), 819–826.

Wang, Y.-H., Lau, Y.M. & Gao, Y., 2014. Examining the mechanisms of sand creep using DEM simulations, *Granul. Matter,* **16**(5), 733–750.

Wong, R.C.K., 2003. Strain-induced anisotropy in fabric and hydraulic parameters of oil sand in triaxial compression, *Can. Geotech. J.,* **40**(3), 489–500.

Woodruff, W.F., Revil, A., Prasad, M. & Torres-Verdín, C., 2015. Measurements of elastic and electrical properties of an unconventional organic shale under differential loading, *Geophysics,* **80**(4), D363–D383.

Yimsiri, S. & Soga, K., 2010. DEM analysis of soil fabric effects on behaviour of sand, *Geotechnique,* **60**(6), 483–495.

Zhang, Z. & Wang, Y.-H., 2015. Three-dimensional DEM simulations of monotonic jacking in sand, *Granul. Matter,* **17**(3), 359–376.